Journal of Building Engineering 98 (2024) 111064

Contents lists available at ScienceDirect

Journal of Building Engineering

journal homepage: www.elsevier.com/locate/jobe

Deterioration of fire resistance of ultra-high-performance polypropylene-fibre-reinforced concrete (UHPPFRC) under long-term acid rain corrosion action

Boran Zhang [a], Xiaoshan Lin [b], Y.X. Zhang [c], Lihai Zhang [a,*]

[a] Department of Infrastructure Engineering, The University of Melbourne, VIC, 3010, Australia
[b] School of Engineering, RMIT University, 124 La Trobe Street, VIC, 3000, Australia
[c] School of Engineering, Design and Built Environment, Western Sydney University, Kingswood, NSW, 2751, Australia

ARTICLE INFO

Keywords:
Ultra-high-performance polypropylene fibre reinforced concrete
Aging effect
Sulphate attack
Fire resistance
Probability of failure

ABSTRACT

The application of ultra-high-performance polypropylene-fibre-reinforced concrete (UHPPFRC) has become widespread due to its superior mechanical properties and non-flammable characteristic. Compared to UHPC, the fire resistance of UHPPFRC, which is crucial in ensuring structural integrity and safety during fire incident, has been improved by the addition of PP fibres. In recent years, the escalation of industrial emission has resulted in a more pronounced pollution of acid rain, a major type of sulphate attack on outdoor concrete structures, leading to the aging of UHPPFRC. Given the long service life of civil engineering structures, the fire performance of aging UHPPFRC should be given significant consideration, yet few studies have taken it into account. This study, for the first time, analyses the deterioration of fire resistance of acid-rain-induced aging UHPPFRCs and compares their probability of failure under fire condition across different corrosion durations, providing guidance for the maintenance of UHPPFRC in acid-rain-prone areas. A novel coupled chemo-thermal-mechanical model is developed, which is employed to investigate the sulphate penetration process and internal stress development within UHPPFRC during the corrosion stage, and to predict temperature and internal stress distribution during the subsequent heating stage. The effects of sulphate concentration, heating rate and fibre dosage on the probability of failure of aging UHPPFRC are then studied. The results obtained from the numerical investigation indicate that the aging effect can significantly compromise the fire resistance of UHPPFRC and augment the probability of failure at elevated temperature. Also, the probability of failure of aging UHPPFRC is more sensitive to changes in sulphate concentration than changes in heating rate.

Nomenclature

ϕ^s	volume fraction of solid phase
ϕ^l	volume fraction of liquid phase
ϕ^g	volume fraction of gas phase
ϕ^v	volume fraction of water vapor

---

* Corresponding author.
E-mail address: lihzhang@unimelb.edu.au (L. Zhang).

https://doi.org/10.1016/j.jobe.2024.111064
Received 13 August 2024; Received in revised form 30 September 2024; Accepted 12 October 2024

ϕ^{f}	volume fraction of liquid water
ϕ^{de}	volume fraction of water dehydrated
ϕ^{pp}	volume fraction of PP fibres
ϕ^{ett}	volume fraction of ettringite
ϕ^{gyp}	volume fraction of gypsum
ϕ^{por}	porosity of the UHPPFRC
ϕ^{por}_{ini}	initial porosity of the UHPPFRC
ϕ^{por}_{res}	residual porosity after corrosion
$f^{tot}_{ck,t}$	initial tensile strength of UHPPFRC
$f^{m}_{ck,t}$	initial tensile strength of cementitious matrix
$f^{pp}_{ck,t}$	initial tensile strength of PP fiber
σ^{tot}_{t}	total internal tensile stress in UHPPFRC
σ^{tot}_{t0}	Initial tensile stress in UHPPFRC
ρ^{p}	density of the paste
ρ^{s}	density of the aggregate
ρ^{w}	density of the water
$\dot{S}^{SO_4^{2-}}$	reaction rate of SO_4^{2-}
$\dot{S}^{ett}$	reaction rate of ettringite
$\dot{S}^{CA}$	reaction rate of calcium aluminate
$\dot{S}^{gyp}$	reaction rate of gypsum
$\dot{S}^{ev}$	mass sink of liquid water due to evaporation
$\dot{S}^{de}$	mass formation of liquid water caused by bound water releasing into pores
$c_{SO_4^{2-}}$	concentration of SO_4^{2-}
k_1, k_2	chemical reaction rate
D^{0}_{eff}	initial effective diffusion coefficient
D_{eff}	effective diffusion coefficient
γ_1	the content of each aluminate phase
h_{α}	the degree of cement hydration
M_i	molar mass of each phase
c_p	the total concentration of reaction products
c_{gyp}	solid-based concentration of gypsum
c_{ett}	solid-based concentration of ettringite
$\overline{c_{gyp}}$	matrix-based concentration of gypsum
$\overline{c_{ett}}$	matrix-based concentration of ettringite
f_{vc}	volume fraction of cement
λ_d	specific heat of dehydration
λ_e	specific heat of evaporation
$\dot{S}^{p}$	the mass change caused by the reaction consuming aluminate phase
$\dot{S}^{gyp}$	mass formation of gypsum
$\dot{S}^{ett}$	mass formation of ettringite
σ^{s}_{t}	increase of internal tensile stress at corrosion stage
σ^{h}_{t}	increase of internal tensile stress at heating stage
σ^{th}_{t}	thermal stress
ε	total strain within UHPPFRC
ε_s	sulphate-attack-induced strain
ε_{th}	thermal strain
$\dot{\varepsilon_{th}}$	changing rate of thermal strain
$\varepsilon_{ck,t}$	elastic strain limit of UHPPFRC
$\dot{T}$	changing rate of temperature
P_g	pore pressure
P_v	vapor pressure
P_{sat}	saturation vapor pressure
J^{l}	mass flux of liquid water transferred by convection
J^{v}	mass flux of water vapor transferred by convection
u	displacement vector
α	coefficient of thermal expansion

$\boldsymbol{\delta_{ij}}$	Kronecker delta
$\boldsymbol{b}$	body force
$\boldsymbol{P_f}$	failure probability of the UHPPFRC
$\boldsymbol{m^i}$	mass content of phase *i* within UHPPFRC (*i*=*s, l, g …*)
$\boldsymbol{\alpha_B}$	Biot coefficient
$\boldsymbol{K}$	intrinsic permeability of UHPPFRC
$\boldsymbol{K^g}$	permeability index
$\boldsymbol{v^g}$	velocity of gas phase
$\boldsymbol{v^l}$	velocity of liquid water
$\boldsymbol{R^v}$	gas constant for water vapor
$\boldsymbol{V}$	volume of UHPPFRC
$\boldsymbol{k_{eff}}$	thermal conductivity of UHPPFRC
$(\rho \boldsymbol{C})_{con}$	heat capacity of UHPPFRC

1. Introduction

Ultra-high-performance concrete (UHPC), known for its excellent mechanical properties at room temperature and non-combustibility [1,2], is now widely used in infrastructure engineering. Fire, as a destructive hazard to buildings, can cause severe cracking and spalling of construction materials like UHPC, resulting in strength degradation and even failure [3–7]. In recent years, there have been an increasing number of high-rise building fires, which could rapidly spread upwards along the building's exterior due to the extensive use of combustible composite materials. Compared to normal strength concrete, the denser microstructure of UHPC can cause greater pore pressure within pores, making it more susceptible to cracking and spalling at elevated temperature [8,9]. To enhance its fire performance, polypropylene (PP) fibre has been employed to reinforce UHPC (UHPPFRC) [10,11]. The melt of PP fibres under high temperature can provide more pathways for water vapor within UHPPFRC, significantly mitigating internal pore pressure, thereby protecting concrete against cracking and spalling and improving the tensile property [12,13].

Studies about permeability and pore pressure were carried out to further understand the spalling-mitigation mechanism of PP fibre [14–16], among which several experiments were based on the previous research conducted by Kalifa et al. [15]. These experiments have confirmed that during the heating process, the permeability and pore pressure within HPPFRC keep changing due to the phase change of PP fibre during heating. Li et al. [16] experimentally and numerically investigated the pore pressure, thermal stress and explosive spalling within UHPPFRC at elevated temperature. It was proved that thermal stress, rather than pore pressure, was the primary factor in initiating UHPPFRC cracking, and PP fibre can mitigate pore pressure within UHPPFRC to some extent. Some numerical studies were also conducted to predict the build-up pore pressure based on heat and moisture transfer theories [9,17–23].

However, UHPPFRC structures, given the long design life, are susceptible to various long-term erosion including sulphate attack, which can significantly compromise their strength and fire resistance [24–26]. The rapid increase of industrial emission has resulted in a more pronounced pollution of acid rain, a major type of sulphate attack on outdoor structures [27,28]. The presence of chemical components like gypsum and ettringite, resulting from the reaction of sulphate ions with the cementitious matrix, leads to the development of expansive internal stress and reduced porosity. The accumulation of internal expansive stress and the decrease in porosity within UHPPFRC can gradually impair its residual tensile strength at ambient temperature and increase pore pressure at elevated temperature, thereby further compromising its fire resistance. The erosion-induced structural vulnerabilities can make aging UHPPFRC more susceptible to cracking, spalling or even failure during fire incidents, posing significant risks to the safety of buildings and occupants. The impact of acid rain on UHPPFRC durability is particularly evident in structures in long-term exposure scenarios. Therefore, the fire behaviour of aging UHPPFRC at elevated temperature should be carefully evaluated. To date, however, brand-new UHPPFRC specimens were used in most studies associated with fire resistance, where the aging effect on UHPPFRC has not been studied yet.

With regard to concrete subjected to sulphate attack, its mechanism was investigated by Liu et al. [29], and the experimental results demonstrated that, instead of salt crystallization, large amounts of ettringite, gypsum and brucite were found and identified as the cause of concrete failure. A classical theoretical model, which characterised the reactive-diffusion process and mechanical deterioration within concrete, was first proposed by Tixier and Mobasher [30,31]. It has been further modified with the consideration of the effects of different factors on external sulphate attack [32–38]. For instance, a meso-level model was developed by Idiart et al. [35] to predict the cracking effect on concrete degradation under sulphate attack. Based on the classical model, Qin et al. [38] established a chemo-transport-damage model to investigate the effects of calcium leaching and temperature on sulphate attack, emphasizing the importance of considering calcium leaching and porosity change. Although extensive simplified theoretical models have been proposed in this field, not a unified theory has been developed because of the complex deterioration processes.

The theory of porous media has been utilized to model the aging process within concrete [25,32,39]. Previous studies revealed that the time-and-space dependent reaction products can cause the porosity change, which then further causes internal expansive stress, change of diffusion coefficients and failure of concrete [29,40]. Sun et al. [25] developed a coupled chemo-mechanical model using pore-elastic theory to predict the elastic deformation of conventional concrete under sulphate attack, and the study indicated that the internal expansive stress started to increase rapidly when the normalized ettringite concentration reached 20 %. It was found by Sun et al. [41] that the time for concrete to reach the reliability index limit state was significantly shortened with the increase of sulphate concentration. In summary, the fire resistance of aged UHPPFRC induced by acid rain has not been thoroughly studied. Specifically, the variations in porosity and internal expansive stress throughout the entire strength reduction process, which involves long-term corrosion and exposure to fire shock, have not been adequately investigated.

In this study, a coupled chemo-thermal-mechanical model is developed to investigate the fire resistance of acid-rain-induced aging UHPPFRC panels. Focusing on high-rise fires which can rapidly spread upwards from the building's exterior, the fire behaviour of aging UHPPFRC panels exposed to fire and corrosion on the same side is studied. The model incorporates the diffusion-reaction behaviour of sulphate ions, the theory of porous media and Hill function with updated factors. It takes into account the changes in porosity, the internal stress that accumulates during the corrosion stage, as well as the reduction in tensile strength of UHPPFRC due to PP fibres melting. Finally, to explore the effects of different factors (*i.e.*, sulphate concentration, heating rate and fibre dosage) on the probability of failure and crack propagation of the aging UHPPFRC panels, a parametric study is conducted on corrosion duration and sulphate concentration. Given the complex deterioration process of UHPPFRC, this study primarily focuses on the linear elastic stage of UHPPFRC at elevated temperatures to provide an initial insight into its underlying mechanism. Once the UHPPFRC panel reaches its elastic strain limit, cracks begin to form. This results in a permanent decrease in tensile strength, necessitating a reassessment of the overall structural reliability. Therefore, the prediction of the critical point of the linear elastic phase in UHPPFRC panels can offer valuable insights into the extent of damage in aging UHPPFRC panels at elevated temperatures. This, in turn, aids in evaluating the fire resistance of aging structures with varying degrees of corrosion.

2. Theoretical model

In the present model, the acid-rain-induced reactions and the corresponding internal expansive stress within UHPPFRC are firstly described using the theory of porous media and Hill Function, where the properties of UHPPFRC are updated with consideration of the effect of reaction products on its porosity and residual tensile strength. Following this, the coupled heat and moisture transfer in UHPPFRC at heating stage is described by a set of equations that include mass, energy, and linear momentum conservation. The present model is able to predict the temperature, pore pressure, and stress distribution in aging UHPPFRC by solving this set of equations [42,43]. During this process, further reduction in tensile strength and increase in porosity due to melting of fibres are taken into account. The following three basic assumptions are made in the proposed model, which are in line with those employed in other experiments and models [25,41,44,45].

(i) The occurrence of cracking is identified as the failure criterion.
(ii) Acid rain exposure is regarded as continuous.
(iii) At the corrosion stage, the isotropic expansive stress within the UHPPFRC panel is generated by the accumulation of ettringite in the pore.

The tensile strength of UHPPFRC $f_{ck,t}^{tot}$ consists of tensile strength of cementitious matrix $f_{ck,t}^{m}$ and tensile strength of PP fibres $f_{ck,t}^{pp}$. Their tensile strengths both decrease over temperature, where the tensile strength of PP fibre gradually decreases to zero due to its failure at high temperature.

Previous studies [12,46] propose that PP fibre starts melting at about 165°C and vaporising over 341°C. Therefore, the residual tensile strength of PP fibres over temperature is regarded as a piecewise function in this study and given by

Table 1
List of main parameters in the present model.

Parameter	Value	Reference
Degree of cement hydration h_α	0.50	[82]
Volume fraction of cement	0.45	[25]
Initial diffusion coefficient of SO_4^{2-} in water D_0	$1.07 \times 10^{-9}\ [m^2/s]$	[25]
Chemical reaction rate k_1	$3.05 \times 10^{-8}\ \left[m^3 \cdot mol^{-1} \cdot s^{-1}\right]$	[25,83]
Chemical reaction rate k_2	$1.22 \times 10^{-9}\ \left[m^3 \cdot mol^{-1} \cdot s^{-1}\right]$	[25,83]
Initial concentration of Ca^{2+}	$21.25\ [mol/m^3]$	[25]
Specific heat C_s	$900 + 80\left(\frac{T}{120}\right) - 4\left(\frac{T}{120}\right)^2\ [J/(kg \cdot K)]$	[16,20]
Water vapor constant R_v	$461.5\ [J/(kg \cdot K)]$	[20,21]
Heat transfer convection coefficient h_q	$25\ [W/(m^2 \cdot K)]$	[20,21]
Thermal conductivity k_{eff}	$2 - 0.24\left(\frac{T}{120}\right) + 0.012\left(\frac{T}{120}\right)^2\ [W/(m \cdot K)]$	[16,21,84]
Specific enthalpy of evaporation λ_E	$2.672 \times 10^5 (647.3 - T)^{0.38}\ [J/kg]$	[20]
Specific enthalpy of dehydration λ_D	$2.4 \times 10^6\ [J/kg]$	[20]
Coefficient of thermal expansion	1×10^{-5}	[85]
Tensile strength of the matrix	9.6 [MPa]	[23]
Tensile strength of PP fibre	600 [MPa]	[12]

$$f_{ck,t}^{pp} = f_{ck,0}^{pp} \times \begin{cases} (1.1 - 0.005T), T < 165^\circ C \\ (0.5328125 - 0.0015625T), 165^\circ C \le T \le 341^\circ C \end{cases} \tag{1}$$

where $f_{ck,0}^{pp}$ is the initial tensile strength of PP fibre, and T is the temperature ($^\circ C$) [9].

As for the tensile strength of matrix $f_{ck,t}^{m}$, its degradation process over temperature can be defined by Eq. (2) as reported in Ref. [47].

$$f_{ck,t}^{m} = f_{ck,0}^{m} \times \left(1 - \frac{T-20}{800}\right) \tag{2}$$

where $f_{ck,0}^{m}$ is the tensile strength of matrix at room temperature. The values of $f_{ck,0}^{pp}$ and $f_{ck,0}^{m}$ are listed in Table 1.

Fig. 1 shows the tensile capacity change of UHPPFRC after long-term acid rain induced sulphate attack. The horizontal axis represents time, and the vertical axis represents normalized time-dependent tensile stress within UHPPFRC $\sigma_t^{tot}(t)/f_{ck,t}^{tot}\ (t)$, where $f_{ck,t}^{tot}\ (t)$ is the time-dependent tensile capacity of UHPPFRC, and $\sigma_t^{tot}(t)$ is the time-dependent total tensile stress which can be described as the sum of the internal tensile stress $\sigma_t^{s}(t)$ caused by sulphate attack and the internal tensile stress $\sigma_t^{h}(t)$ induced by elevated temperature. The initial tensile stress of UHPPFRC σ_{t0} equals to 0. With the gradual penetration of sulphate ions over time, ettringite is generated within UHPPFRC, causing the increase of normalized internal tensile stress $\Delta\sigma_t^{s}(t)/f_{ck,t}^{tot}\ (t)$. When UHPPFRC undergoes a fire incident (as indicated by the red vertical line in Fig. 1) at a specific time t, its normalized internal tensile stress experiences a further increase by $\Delta\sigma_t^{h}(t)/f_{ck,t}^{tot}\ (t)$, and this occurs within a short period time due to the rapid increase of thermal stress and pore pressure. The remaining tensile strength of UHPPFRC is governed by a probability distribution based on structure reliability method [41,48].

The time-dependent performance function can be expressed by using two factors, namely the elastic tensile strength $f^{tot}\ (t)$ and the internal tensile stress within the UHPPFRC panel $\sigma^{tot}(t)$.

$$Z(t) = ftot\ (t) - \sigma tot(t) = g(X, t) = g(X_1, X_2, \ldots, X_n, t) \tag{3}$$

where X_n represents the vector of n-th random variables that related to the performance of concrete. Therefore, the probability of failure can be defined as

$$p_f = P(Z < 0) = 1 - \phi(\beta) \tag{4}$$

where $\phi(\cdot)$ represents the standard normal distribution function and β represents the reliability index. The mean and the standard deviation of n-th variables are defined as μ_n and σ_n, respectively. By using Taylor series expansion, the performance function is expressed as [49],

$$Z = g(\mu) + \sum_{i=1}^{n} \frac{\partial g}{\partial X_i} + \frac{1}{2} \sum_{i=1}^{n} \sum_{j=1}^{n} \frac{\partial g^2}{\partial X_i \partial X_j} (X_i - \mu_1)(X_j - \mu_2) + \ldots \tag{5}$$

In the current study, other previously occurring environmental factors X_1 and chemical composition of the UHPPFRC panel X_2 are considered as two random variables [41,50]. By applying first-order approximations, the mean and standard deviation of the performance function can be obtained,

$$\mu_z \approx g(X_1, X_2) \tag{6}$$

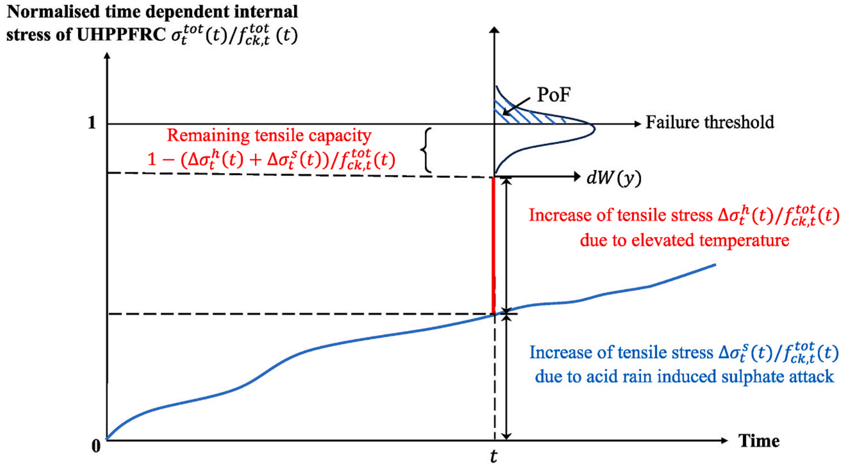

Fig. 1. Fire resistance of UHPPFRC panel after long-term acid rain induced sulphate attack.

$$\sigma_z \approx \frac{1}{2}\sum_{i=1}^{n}\sum_{j=1}^{n}\frac{\partial g^2}{\partial X_i \partial X_j}COV\left(X_i, X_j\right) \approx \sum_{i=1}^{2}\left(\frac{\partial g}{\partial X_i}\right)^2 Var(X_i) \tag{7}$$

where $COV\left(X_i, X_j\right)$ is the covariance of X_i and X_j. Assuming all the variables are statistically independent, the reliability index can be calculated as,

$$\beta = \frac{\mu_z}{\sigma_z} \tag{8}$$

2.1. Tensile stress within UHPPFRC

2.1.1. Tensile stress induced by acid rain

Fig. 2 shows the penetration of sulphate ions from the surface of UHPPFRC into its interior under acid rain condition. As shown in Fig. 2 (a), the UHPPFRC panel is divided into two parts, named sulphate ions penetration zone and uninvaded zone. Fig. 2 (b) describes the generation process of microscale internal expansive stress within a single pore. Solid gypsum and ettringite are subsequently generated in pores by the reactions mentioned above, resulting in the porosity reduction of UHPPFRC and internal expansive stress σ_t^s. The associated chemical reactions are briefly introduced in this section, and the details of stress-related equations can be found in Section 2.2.3.

Experimental investigations [29,51] revealed a strong correlation between the deterioration of concrete strength and the expansion stress caused by the expansive reaction products such as ettringite ($C_6AS_3H_{32}$) and gypsum (CSH_2). Firstly, the reaction between calcium ions and sulphate ions leads to the formation of the secondary gypsum.

$$Ca^{2+} + SO_4^{2-} + 2H \xrightarrow{k_1} C\overline{S}H_2$$

Subsequently, ettringite is formed through the chemical reaction between the secondary gypsum and hydrated calcium aluminates [25,30,52]. That is,

$$C_3A + C\overline{S}H_2 + 26H \rightarrow C_6A\overline{S}_3H_{32}$$

$$C_4AH_{13} + 3C\overline{S}H_2 + 14H \rightarrow C_6A\overline{S}_3H_{32} + CH$$

$$C_4A\overline{S}H_{12} + 2C\overline{S}H_2 + 16H \rightarrow C_6A\overline{S}_3H_{32}$$

$$3C_4AF + 12C\overline{S}H_2 + aH \rightarrow 4C_6A\overline{S}_3H_{32} + 2[(A, F)H_3]$$

The four reactions above can be expressed using one simplified formula as follows [25,35,53,54].

$$CA + nC\overline{S}H_2 \xrightarrow{k_2} C_6A\overline{S}_3H_{32}$$

where k_1 and k_2 are the chemical reaction rates of corresponding equations, respectively [25]. γ_i represents the content of each aluminate phase [32,53]:

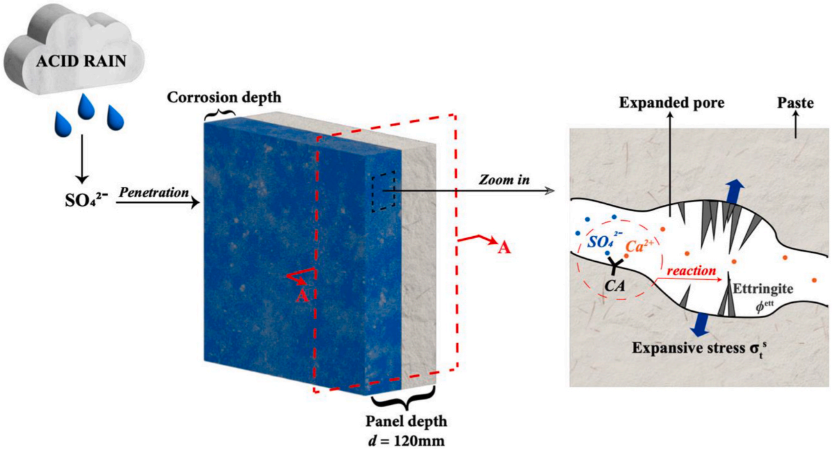

(a) (b)

Fig. 2. Microscale analysis of the UHPPFRC panel subjected to long-term sulphate attack.

$$\gamma_i = \frac{C_{A\_i}}{\sum_i^4 C_{A\_i}}$$

$$\mathrm{n} = 3\gamma_1 + 2\gamma_2 + 3\gamma_3 + 4\gamma_4 = \frac{8}{3}$$

$$CA = \gamma_1 C_3A + \gamma_2 C_4AH_{13} + \gamma_3 C_4A\overline{S}H_{12} + \gamma_4 C_4AF$$

where C_{A_i} is the molar concentration of each aluminate phase.

2.1.2. *Tensile stress induced by elevated temperature*

Under high temperature, the water vapor generated by evaporation of free and bound water within UHPPFRC can cause tensile stress and associated tensile strain. The heat and moisture transfer within the A-A section of the UHPPFRC panel after prolonged exposure to sulphate attack under fire condition is depicted in Fig. 3. As shown in Fig. 3 (a), due to the external elevated temperature T_h, the heat transfers into UHPPFRC from the surface on the left. The temperature gradient, represented by the variation of colour from red to light blue, results in water vapor migration from the surface to the deeper area of UHPPFRC. Once the temperature in a specific region reaches a critical level, the intact fibres in that area start to melt, gradually turning into “damaged fibres”, and eventually becoming “melted fibres”. Fig. 3 (b) depicts the microscale expansive stress generation process within an individual pore. The overall expansive stress in the pore consists of ettringite-induced stress and water-vapor-induced pore pressure, caused by reaction during sulphate attack and elevated temperature during heating, respectively. The volume fraction of water vapor ϕ^v in the pore is primarily influenced by three factors, *i.e.* water vapor flowing from the higher-temperature regions to the pore, water vapor generated by liquid water within the pore, and water vapor releasing from the pore to cooler region. Water vapor accumulates in the pore when inflow exceeds outflow, leading to an increase in pore pressure P_g. Moreover, when the temperature exceeds 200 $^\circ C$, chemical bound water is released from the cementitious matrix, thereby further increasing the volume fraction of liquid water [20,21].

In addition to the pore pressure, thermal stress induced by intense heating can also lead to great thermal expansion. According to Ref. [55], the thermal expansion of all kinds of UHPCs show subtle variation between 20 $^\circ C$ and 500 $^\circ C$, so the coefficient of thermal expansion measured by previous experiments is employed in the present study as shown in Table 1.

2.2. *Governing equations*

The UHPPFRC panel used in the current study can be considered as a mixture of solid phase (*i.e.,* paste and fibre), liquid phase (*i.e.,* free water) and gas phase (*i.e.,* water vapor) at both corrosion and heating stages. The volume fraction of each phase can be defined as,

$$\phi^i = \frac{V^i}{V} \tag{9}$$

where V is the volume of the UHPPFRC panel, i=p, gyp, ett, f, and v, representing the volume fractions of paste, gypsum, ettringite, liquid water and water vapor, respectively.

To simulate the acid rain environment, it is assumed that the external surface of the UHPPFRC panel is initially submerged in the solution with a specific SO_4^{2-} concentration at the beginning of the corrosion stage according to previous experimental settings [25,56,57]. Sulphate ions then penetrate into UHPPFRC and reacts with calcium ions to form gypsum ϕ^{gyp}. Subsequently, solid ettringite ϕ^{ett} is generated in pores by the chemical reaction between secondary gypsum and hydrated calcium aluminates, resulting in a permanent decrease in porosity. When fire shock occurs, temperature increases due to heat transfer, and water vapor is gradually generated in

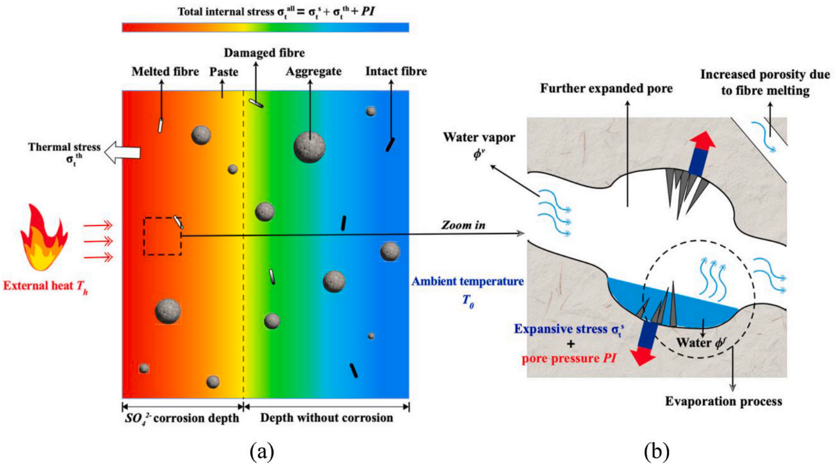

Fig. 3. Microscale analysis of the UHPPFRC panel subjected to elevated temperature after long-term sulphate attack.

pores by evaporation. It is assumed that the summation of the volume fractions of solid ϕ^s (*i.e.* paste ϕ^p, gypsum ϕ^{gyp} and ettringite ϕ^{ett}), liquid ϕ^l (*i.e.* liquid water ϕ^f) and gas ϕ^g (*i.e.* water vapor ϕ^v) phases is equal to 1, given as

$$\phi^s + \phi^l + \phi^g = 1 \tag{10}$$

$$\phi^s = \phi^p + \phi^{gyp} + \phi^{ett} \tag{11}$$

ϕ^{por}_{res} is the residual porosity of UHPPFRC after sulphate attack as given in Eq. (12).

$$\phi^{por}_{res} = \phi^{por}_{ini} - (\phi^{gyp} + \phi^{ett}) \tag{12}$$

where ϕ^{por}_{ini} is the initial porosity of UHPPFRC prior to sulphate penetration. According to Ref. [25], it can be expressed by

$$\phi^{por}_{ini} = f_{vc}\frac{w/c - 0.36h_\alpha}{w/c + 0.32} \tag{13}$$

where h_α is the degree of cement hydration. f_{vc}, the volume fraction of cement in concrete, which can be determined by Ref. [58]:

$$f_{vc} = \frac{1}{1 + \frac{\rho^p}{\rho^s}s_c + \frac{\rho^p}{\rho^w}w_c} \tag{14}$$

where ρ^p, ρ^s, and ρ^w represent the densities of cement, aggregate and water, respectively. s_c and w_c are the aggregates-to-cement mass ratio and water-to-cement mass ratio, respectively.

At heating stage, the porosity of UHPPFRC should be always equal to the summation of the volume fractions of liquid phase and gas phase.

$$\phi^{por} = \phi^l + \phi^g \tag{15}$$

Where the temperature dependent ϕ^{por} can be further described as

$$\phi^{por} = \phi^{por}_{res}\begin{cases} 1, T < 100^\circ C \\ aT^3 + bT^2 + cT + d, 100^\circ C \le T \le 800^\circ C \\ 3, T > 800^\circ C \end{cases} \tag{16}$$

where a, b, c and d are the coefficients of a cubic function so that ϕ^{por} and its temperature derivative are continuous [25]. With consideration of the melt of PP fibres during the heating process, the ultimate porosity can be expressed as,

$$\phi^{por} = \begin{cases} \phi^{por}_{res}, T < 165^\circ C \\ \phi^{por}_{res} + \phi^{pp}, T \ge 165^\circ C \end{cases} \tag{17}$$

In the present study, only the transfer of water vapor is considered at elevated temperature. Liquid water is regarded as a static phase, and the effect of dry air within UHPPFRC at elevated temperature is ignored. This method, adopted by Dwaikat et al. [59], is considered to be reasonable because permeability of liquid water in concrete is much smaller than that for water vapor, and the mass of dry air is small compared to the mass of water during heating.

2.2.1. *Conservation of mass*

The mass conservation of each phase could be expressed as

$$\frac{\partial m^i}{\partial t} + \nabla \cdot \boldsymbol{J}^i = \dot{S}_i \tag{18}$$

where m^i is the mass content of phase i within UHPPFRC. $\partial m^i/\partial t$ represents the rate of phase change in a unit volume of UHPPFRC. $\boldsymbol{J}^i$ is the mass flux of phase i transferred by convection. $\dot{S}_i$ represents the mass sink or mass formation of phase i, which is a partial derivative of mass change to time.

$$m^i = \rho^i\phi^i = \overline{c_i}M_i \tag{19}$$

where ρ^i is the density of each phase, ϕ^i representing the volume fraction, $\overline{c_i}$ the matrix based molar concentration of each phase, and M_i the molar mass of each phase.

$$\boldsymbol{J}^i = \rho^i\phi^i\boldsymbol{v}^i \tag{20}$$

where $\boldsymbol{v}^i$ is the velocity of each phase.

2.2.1.1. Mass conservation of solid phase. In the current study, the solid phase within UHPPFRC consists of paste, gypsum and ettringite. Their conservation of mass can be expressed as.

Paste:

$$\frac{\partial(\rho^p\phi^p)}{\partial t}+\nabla\cdot\rho^p\phi^p\boldsymbol{v}^p=\dot{S}^p \tag{21}$$

Gypsum:

$$\frac{\partial(\rho^{gyp}\phi^{gyp})}{\partial t}+\nabla\cdot\rho^{gyp}\phi^{gyp}\boldsymbol{v}^{gyp}=\dot{S}^{gyp} \tag{22}$$

Ettringite:

$$\frac{\partial(\rho^{ett}\phi^{ett})}{\partial t}+\nabla\cdot\rho^{ett}\phi^{ett}\boldsymbol{v}^{ett}=\dot{S}^{ett} \tag{23}$$

where ϕ^p, ϕ^{gyp}, and ϕ^{ett} represent the density of paste, gypsum and ettringite, respectively. Under static condition, the velocity of paste, gypsum and ettringite relative to a fixed REV equal to zero [25]. $\dot{S}^p$, $\dot{S}^{gyp}$, and $\dot{S}^{ett}$ represent the mass change caused by the mass sink of cementitious paste, and due to the reaction and formation of gypsum and ettringite, respectively.

The volume fraction of gypsum and ettringite can be expressed as

$$\phi^{gyp}(z,t)=\frac{\overline{c_{gyp}}M_{gyp}}{\rho^{gyp}}=\frac{c_{gyp}M_{gyp}\phi^s}{\rho^{gyp}} \tag{24}$$

$$\phi^{ett}(z,t)=\frac{\overline{c_{ett}}M_{ett}}{\rho^{ett}}=\frac{c_{ett}M_{ett}\phi^s}{\rho^{ett}} \tag{25}$$

By substituting Eqs. (10), (24) and (25) into Eqs. (22) and (23), the mass conservation equations become (ϕ^g equals to zero during the sulphate attack because no water vapor generated under room temperature)

$$\frac{\partial\left(\mathrm{c_{gyp}M_{gyp}}\left(1\text{-}\phi^{f}\right)\right)}{\partial \mathrm{t}}+\nabla\cdot\left(\mathrm{c_{gyp}M_{gyp}}\left(1\text{-}\phi^{f}\right)\right)\mathbf{v}^{\mathrm{gyp}}=\dot{\mathrm{S}}^{\mathrm{gyp}} \tag{26}$$

$$\frac{\partial\left(\mathrm{c_{ett}M_{ett}}\left(1\text{-}\phi^{f}\right)\right)}{\partial \mathrm{t}}+\nabla\cdot\left(\mathrm{c_{ett}M_{ett}}\left(1\text{-}\phi^{f}\right)\right)\mathbf{v}^{\mathrm{ett}}=\dot{\mathrm{S}}^{\mathrm{ett}} \tag{27}$$

2.2.1.2. Mass conservation of solute phase. Previous studies have revealed the mechanism of solute transport in deforming porous media [42,43,60,61]. According to the ions transport equation derived by Sun et al. [25], the mass conservation of the sulphate ions can be described as

$$\frac{\partial c_{SO_4^{2-}}\phi^f}{\partial t}+\nabla\cdot\boldsymbol{J}^{SO_4^{2-}}=-\dot{S}^{SO_4^{2-}} \tag{28}$$

where $c_{SO_4^{2-}}$ represents fluid-based concentration of sulphate ions, $\boldsymbol{J}^{SO_4^{2-}}$ the mass flux of sulphate ions, and $\dot{S}^{SO_4^{2-}}$ the SO_4^{2-} ions concentration sink due to chemical reaction.

The reactive transport process consists of diffusion and reaction, where the former could be described by Fick's second law. Therefore, the mass flux of sulphate ions in the fluid phase is derived as

$$\boldsymbol{J}^{SO_4^{2-}}=-D_{eff}\nabla c_{SO_4^{2-}}\phi^f+\boldsymbol{v}^f c_{SO_4^{2-}}\phi^f \tag{29}$$

where D_{eff} represents the effective diffusion coefficient [62,63], and it changes over time due to the filling effect of reaction products, namely gypsum and ettringite. Its relationship with the reaction processes can be expressed by the initial effective diffusion coefficient D^0_{eff}, concentrations of gypsum and ettringite, and two parameters α and q representing the filling effect of reaction products on D_{eff}:

$$\frac{\mathrm{D_{eff}}}{\mathrm{D^0_{eff}}}=\exp\left[\alpha\left(-\frac{\mathrm{c_p}}{\mathrm{q}\cdot\mathrm{c_p^{max}}}\right)\right] \tag{30}$$

where c_p represents the total concentration of reaction products (*i.e.* c_{gyp} and c_{ett}), and c_p^{max} represents the maximum possible concentration of reaction products [54]. α and q are constants given in Ref. [61]. D^0_{eff} depends on the characteristics of pore structure in material [25] and can be described by

$$D^0_{eff}=D_0\phi^{por}_{ini}\tau=D_0\frac{2\phi^{por}_{ini}}{3-\phi^{por}_{ini}} \tag{31}$$

$$\tau=\frac{2}{3-\phi^{por}_{ini}} \tag{32}$$

where D_0 represents the initial diffusion coefficient of sulphate ions in water and τ is the tortuosity [25].

According to the chemical reactions within UHPPFRC at corrosion stage, sulphate ions react with Ca^{2+} to form gypsum, followed by the generation of ettringite caused by chemical reaction between secondary gypsum and hydrated calcium aluminates. The reaction rates of SO_4^{2-}, ettringite, $C3A$ and gypsum in this process can be respectively expressed by the following equations [53,54]

$$\dot{S}^{SO_4^{2-}} = k_1 \cdot c_{Ca^{2+}} \cdot c_{SO_4^{2-}} \tag{33}$$

$$\dot{S}^{ett} = k_2 \cdot {c_{gyp}}^{n} \cdot c_{CA} \tag{34}$$

$$\dot{S}^{CA} = -k_2 \cdot {c_{gyp}}^{n} \cdot c_{CA} \tag{35}$$

$$\dot{S}^{gyp} = k_1 \cdot c_{Ca^{2+}} \cdot c_{SO_4^{2-}} - n \cdot k_2 \cdot {c_{gyp}}^{n} \cdot c_{CA} \tag{36}$$

where $c_{Ca^{2+}}$ represents the constant calcium concentration at saturated solution, and c_{CA} represents the concentration of hydrated calcium aluminates reacting with secondary gypsum.

2.2.1.3. Mass conservation of liquid phase. During the sulphate attack stage, mass conservation of liquid water can be defined as

$$\frac{\partial(\rho^f \phi^f)}{\partial t} + \nabla \cdot \left(\rho^f \phi^f \boldsymbol{v}^f\right) = \dot{S}^f \tag{37}$$

where $\dot{S}^f$ represents the mass change due to chemical consumption and partial substitution of ettringite. The volume sink of water should be equal to the volume formation of gypsum and ettringite, so the time and depth dependent volume fraction of liquid phase can be expressed as

$$\phi^f(z,t) = \phi_{ini}^{por} - \left(\frac{c_{gyp} M_{gyp} \phi^s}{\rho^{gyp}} + \frac{c_{ett} M_{ett} \phi^s}{\rho^{ett}}\right) \tag{38}$$

Subsequently, mass conservation of liquid water during fire can be expressed as

$$\frac{\partial(\rho^f \phi^f)}{\partial t} + \nabla \cdot \left(\rho^f \phi^f \mathbf{v}^f\right) = \dot{S}^{de}\text{-}\dot{S}^{ev} \tag{39}$$

where $\dot{S}^{de}$ is the mass of liquid water formed by dehydration process at elevated temperatures, and $\dot{S}^{ev}$ the mass sink of liquid water due to evaporation.

As the mobility of liquid is negligible compared to that of gas [59], in the present study, it is assumed that $\boldsymbol{v}^f = 0$.

Thus, the conservation of liquid water becomes

$$\frac{\partial(\rho^f \phi^f)}{\partial t} = \dot{S}^{de} - \dot{S}^{ev} \tag{40}$$

2.2.1.4. Mass conservation of gas phase. In the current study, the effect of dry air is ignored at elevated temperature, so the gas phase consists of water vapor only [9,59]. Water vapor is generated by the evaporation of liquid water in pores. The conservation of water vapor mass within UHPPFRC can be defined as

$$\frac{\partial(\rho^v \phi^v)}{\partial t} + \nabla \cdot \boldsymbol{J}^v = \dot{S}^{ev} \tag{41}$$

The mass flux of water vapor $\boldsymbol{J}^v$ can be expressed in terms of pressure and concentration of gradients, assuming that Fick's and Darcy's laws are applicable [20,21].

$$\boldsymbol{J}^v = \rho^v \phi^v \boldsymbol{v}^g - \rho^v \phi^g D_{AV} \nabla\left(\frac{\rho^v \phi^v}{\rho^v \phi^g}\right) \tag{42}$$

$$\boldsymbol{v}^g = -\frac{K K^g}{\mu^g} \nabla P_g \tag{43}$$

where $\boldsymbol{v}^g$ is the velocity of gas, μ^g the dynamic viscosity of gas, P_g the pore pressure, K the intrinsic permeability of UHPPFRC [23], and K^g the permeability index defined as a function related to saturation of liquid water

$$K^g = 1 - \phi^l / \phi^{por} \tag{44}$$

Substituting Eq. (42) and Eq. (43) into Eq. (41) leads to

$$\frac{\partial(\rho^v \phi^v)}{\partial t} - \nabla \cdot \left(\rho^v \phi^v \frac{K K^g}{\mu^g} \nabla P_g - \rho^g \phi^g D_{AV} \nabla\left(\frac{\rho^v \phi^v}{\rho^v \phi^g}\right)\right) = \dot{S}^{ev} \tag{45}$$

In the present study, water vapor is assumed to behave as ideal gas, so its partial density and pressure can be expressed by ideal gas law as

$$P_v = R^v \rho^v T \tag{46}$$

Since the transfer and expansion of dry air are ignored in this study [59], $P_g = P_v$, $\phi^g = \phi^v$. Therefore, the final equation for water vapor conservation can be written as

$$\frac{\partial(\rho^v \phi^v)}{\partial t} - \nabla \cdot \left(\rho^v \phi^v \frac{KK^g}{\mu^g} \nabla R^v \rho^v T \right) = \dot{S}^{ev} \tag{47}$$

2.2.2. *Conservation of energy*

In the current study, Fourier's law is introduced to define the energy conservation of a pore at elevated temperature (*i.e.* at the heating stage)

$$(\rho C)_{con} \frac{\partial T}{\partial t} = -\nabla \cdot \left(-k_{eff} \nabla T\right) - \left(\rho^i C^i \boldsymbol{v}\right) \cdot \nabla T - \lambda_e \dot{S}^{ev} - \lambda_d \dot{S}^{de} \tag{48}$$

where $(\rho C)_{con}$ is the heat capacity of UHPPFRC, T the temperature, and k_{eff} the thermal conductivity of UHPPFRC. λ_e and λ_d are the specific heat of evaporation and the specific heat of dehydration, respectively. $\left(\rho^i C^i \boldsymbol{v}\right)$ relates to the energy transferred by water vapor.

$$\rho^i C^i \boldsymbol{v} = \rho^v \phi^v C^v \boldsymbol{v}^g \tag{49}$$

where $\rho^v \phi^v$ represents the volume fraction of water vapor in matrix. According to Tenchev [21], $\left(\rho^i C^i \boldsymbol{v}\right)$ should be used if the thermal conductivity is determined experimentally for absolutely dry concrete. Otherwise, the effect of the convective transfer is represented by the temperature dependency of thermal conductivity. Since effective thermal conductivity k_{eff} used in the current study is temperature dependent, $\left(\rho^i C^i \boldsymbol{v}\right)$ in Eq. (48) can be considered as zero [20,21,64]

$$(\rho C)_{con} \frac{\partial T}{\partial t} + \nabla \cdot \left(-k_{eff} \nabla T\right) = -\lambda_e \dot{S}^{ev} - \lambda_d \dot{S}^{de} \tag{50}$$

2.2.3. *Conservation of linear momentum*

2.2.3.1. Sulphate corrosion stage. According to previous studies [25,30,34,35,65], the crystallization stress resulting from the accumulation of ettringite would exert on the walls of pores. With the consideration of the complicated and unclear influence of gypsum on the expansion of UHPPFRC, the current study mainly considers the internal expansive stress caused by the crystallization of ettringite [25]. The accumulation of ettringite in a REV of UHPPFRC generates an isotropic internal stress $\boldsymbol{\sigma_{ett}}$ in the microscopic scale, and the governing equation is

$$\nabla \boldsymbol{\sigma} + \boldsymbol{\sigma_{ett}} = \mathbf{C} : \varepsilon_e + \boldsymbol{\sigma_{ett}} = \rho \frac{\partial^2 \boldsymbol{u}}{\partial t^2} \tag{51}$$

where $\boldsymbol{\sigma}$ is Cauchy stress tensor, $\mathbf{C}$ the fourth-order stiffness tensor of cementitious matrix, ε_e the infinitesimal strain tensor and $\boldsymbol{u}$ the displacement vector. By assuming the quasi-static loading condition, Eq. (51) can be simplified as,

$$\nabla \boldsymbol{\sigma} + \boldsymbol{\sigma_{ett}} = \mathbf{C} : \varepsilon_e + \boldsymbol{\sigma_{ett}} = 0 \tag{52}$$

During the sulphate corrosion stage, the total stress within UHPPFRC is assumed to consist of both the elastic stress and internal ettringite pressure. According to Sun et al. [25], the conservation of linear momentum can be expressed as

$$\left[\left(\lambda^{eff} + \mu^{eff}\right) \nabla (\nabla \cdot u) + \mu \nabla^2 u \right] + \boldsymbol{\sigma_{ett}} = 0 \tag{53}$$

where λ^{eff} and μ^{eff} are the Lame parameters that can be determined by Young's modulus E and Poisson's ratio ν as follows.

$$\lambda^{eff} = \frac{E\nu}{(1+\nu)(1-2\nu)} \tag{54}$$

$$\mu^{eff} = \frac{E}{2(1+\nu)} \tag{55}$$

These two coefficients may change under the filling effect of reaction products, thereby for simplification, it is assumed that the accumulation of gypsum and ettringite within UHPPFRC has little impact on λ^{eff} and μ^{eff} during the linear elastic deformation stage of UHPPFRC [25].

The relationship between the concentration of ettringite c_{ett} and the corresponding pressure $\boldsymbol{\sigma}_t^s$ at liquid and crystal surface can be described using Hill function [25,66]

$$\boldsymbol{\sigma}_t^s = \frac{V_{max} \left(c_{ett} / c_{ett\_max}\right)^w}{K^w + \left(c_{ett} / c_{ett\_max}\right)^w} \tag{56}$$

where V_{max} is a parameter related to maximum internal expansive stress caused by ettringite, K the "activation coefficient" defining where c_{ett} would lead to an apparent increase of $\boldsymbol{\sigma}_t^s$. As the steepness of Hill function, w normally changes from 1 to 6. The parameters of

Hill Function adopted by Sun et al. [25] are further updated in this study (*i.e.* $V_{max} = 10^7$, $\omega = 2$ and $K = 40\%$), which has a high prediction accuracy of the concentration distribution of sulphate ions and the internal expansive stress within concrete during the corrosion stage.

2.2.3.2. Fire shock stage. During the fire, the increasing concentration of water vapor in UHPPFRC is assumed to generate an isotropic internal stress $P_g\boldsymbol{I}$ in microscopic scale [25]. The total strain ε consists of elastic strain ε_{el} and thermal strain ε_{th} [64].

$$\varepsilon = \varepsilon_{el} + \varepsilon_{th} = \frac{1}{2}\left(\nabla \boldsymbol{u} + \nabla^T \boldsymbol{u}\right) = \begin{bmatrix} \varepsilon_{xx} & \varepsilon_{xy} & \varepsilon_{xz} \\ \varepsilon_{yx} & \varepsilon_{yy} & \varepsilon_{yz} \\ \varepsilon_{zx} & \varepsilon_{zy} & \varepsilon_{zz} \end{bmatrix} \tag{57}$$

where $\boldsymbol{u}$ is the displacement vector. The changing rate of thermal strain $\dot{\varepsilon_{th}}$ can be expressed as

$$\dot{\varepsilon_{th}} = \alpha \dot{T} \delta_{ij} \tag{58}$$

where α is the coefficient of thermal expansion, $\dot{T}$ the rate of temperature change, and δ_{ij} the Kronecker delta.

The total stress inside UHPPFRC $\boldsymbol{\sigma}$ is considered to consist of thermal stress $\boldsymbol{\sigma_{th}}$ and internal pore pressure P_g, and given as

$$\boldsymbol{\sigma} = \boldsymbol{\sigma_{th}} + \alpha_B P_g \boldsymbol{I} \tag{59}$$

where α_B is the Biot coefficient. Therefore, the stress-strain relationship for UHPPFRC can be defined as

$$\nabla \cdot \left(\boldsymbol{\sigma} - \alpha_B P_g \boldsymbol{I}\right) + \boldsymbol{b} = \frac{\partial^2 \boldsymbol{u}}{\partial t^2} \tag{60}$$

where $\boldsymbol{b}$ is the body force [64]. By assuming quasi-static loading condition, $\partial^2 \boldsymbol{u}/\partial t^2$ equals to 0, thus

$$\nabla \cdot \left(\boldsymbol{\sigma} - \alpha_B P_g \boldsymbol{I}\right) + \boldsymbol{b} = 0 \tag{61}$$

2.2.4. Constitutive relationships

To develop a system encompassing mass conservation of each phase, energy conservation and continuum mechanics, the equations presented in the former sections are integrated. To achieve the closure of these equations and to calculate the corresponding variables, the following relationships are required.

According to Refs. [9,20,21], the mass change $\dot{S}^{de}$ caused by dehydration can be expressed by

$$\dot{S}^{de} = \frac{\partial\left(\phi^{de}\rho^{l}\right)}{\partial t} \tag{62}$$

where ϕ^{de} is the volume fraction of dehydrated water and can be expressed by

$$\phi^{de} = \frac{\phi^{s}\rho^{s}}{\rho^{f}} \times \begin{cases} 0 \quad for\ T < 200^{o}C \\ 7.0 \times 10^{-4}(T - 200) \quad for\ 200^{o}C < T < 300^{o}C \\ 0.4 \times 10^{-4}(T - 300) + 0.07 \quad for\ 300^{o}C < T < 800^{o}C \end{cases} \tag{63}$$

Moreover, the volume fraction of liquid water can be calculated by sorption isotherms (curves). The one proposed by Bazant [18], derived by using numerous experimental data, has been widely used in previous papers [20,21,59,67]. Even though it was initially designed for normal strength concrete, Dwaikat and Kodur [59] discussed and used it in their numerical model for HPC, and the corresponding theoretical results were in good agreement with the experimental data. Furthermore, Ren [22] used both Bazant's model and an improved one to investigate the fire behaviour of reactive powder concrete (RPC), a type of cement based ultrahigh-performance concrete (UHPC). The prediction given by two models showed some discrepancies, but they were not evident, indicating that Bazant's model is suitable for concrete with denser structure and lower permeability. Therefore, the sorption isotherm curves proposed by Bazant [18] is employed in the current study and given by Eq. (64). where,

$$\phi^{l}\rho^{l} = \begin{cases} \phi^{s}\rho^{s}\left(\dfrac{P_v}{P_{sat}}\dfrac{\phi_0^{l}\rho^{l}}{\phi^{s}\rho^{s}}\right)^{1/m(T)} \\ \phi_0^{l}\rho^{l}\left[1 + 0.12\left(\dfrac{P_v}{P_{sat}} - 1.04\right)\right] \\ \phi^{l}\rho^{l}(0.96) + \left(\dfrac{P_v}{P_{sat}} - 0.96\right)\dfrac{\phi^{l}\rho^{l}(1.04) - \phi^{l}\rho^{l}(0.96)}{0.08} \end{cases} \tag{64}$$

$$\text{If}, \frac{P_v}{P_{sat}} \le 0.96 \ \text{if}, \frac{P_v}{P_{sat}} \ge 1.04 \ \text{if}, 0.96 < \frac{P_v}{P_{sat}} < 1.04$$

$$m(T) = 1.04 - \frac{(T + 10)^2}{(T + 10)^2 + 22.3(25 + 10)^2} \tag{65}$$

2.3. Procedure for analysing aging UHPPFRC damage at elevated temperatures

Fig. 4 (a) shows the schematic flow chart for the analysis of damage in UHPPFRC under the combined influence of sulphate attack and elevated temperatures. The UHPPFRC initial properties and the concentration of sulphate ions are given as input for the model. The volume fraction of gypsum and ettringite at different depths at time t_0, as well as the corresponding internal expansive stress, are then determined, followed by the updates of porosity and residual tensile strength of UHPPFRC. By using the updated UHPPFRC properties and the external temperature T_h as input, the model can further predict the temperature distribution within UHPPFRC at time $t_1 = t_0 + \Delta t$ and proceeds to determine and compare the residual tensile strength and internal stress within UHPPFRC. If the residual tensile strength is greater, then the model will update the mechanical properties of UHPPFRC and continue to calculate the temperature distribution at the next time step, followed by a new round of comparison between the corresponding residual tensile strength and internal stress. This calculation-comparison process repeats until the internal stress is greater than the residual tensile strength, which is regarded as the sign of structure failure. Given the complex spalling phenomena at elevated temperatures, the current study mainly focuses on the linear elastic stage of UHPPFRC.

2.4. Boundary and initial conditions

Fig. 5 (a)and (b) demonstrate the dimensions, boundary conditions and initial conditions of the established models. Considering the practical engineering applications, the UHPPFRC panel with dimension of 300 × 300 × 120 mm demonstrated in Li [23] is employed, which has a water-to-cement mass ratio of about 0.33 and aggregate-to-cement mass ratio of about 1.35, and its porosity is thereby calculated and set as 0.1 according to Eq. (13). The thickness of the specimen is chosen based on that of concrete panels commonly used in engineering practice. Details of other information required can be found in Table 1.

2.4.1. Boundary conditions in corrosion stage

During the corrosion stage, the concentration of sodium sulphate $c_{SO_4^{2-}}$ at the front surface ABCD is set as

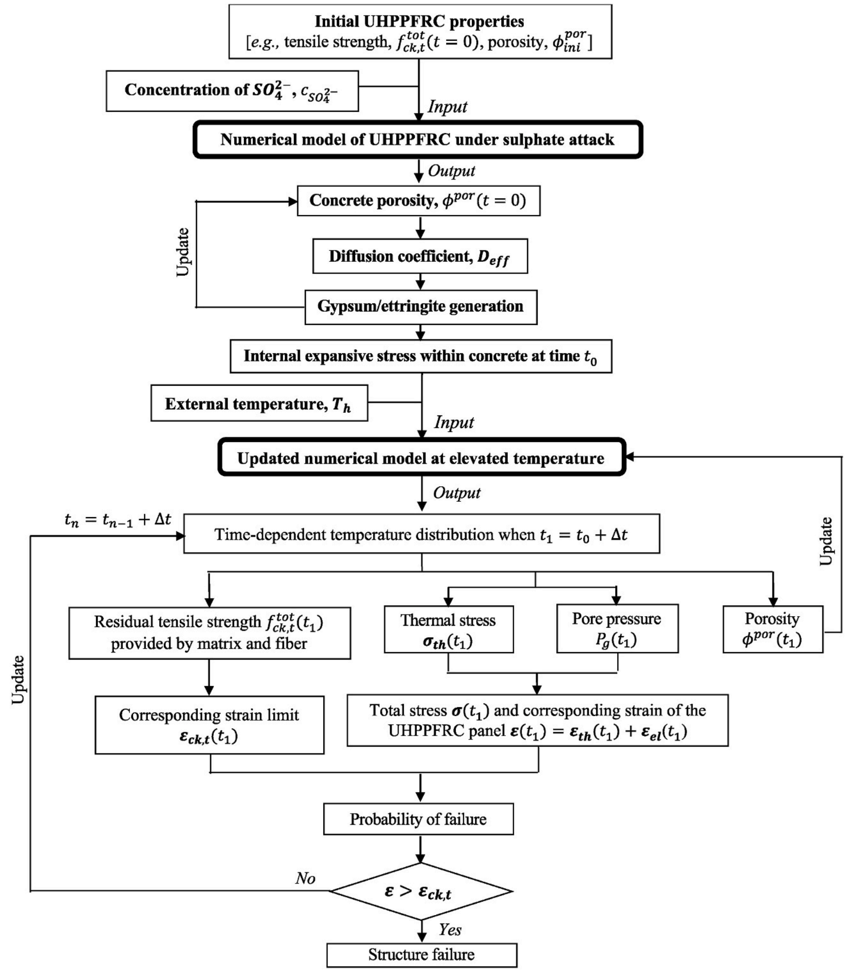

Fig. 4. Schematic flow chart of generation processes of internal stress and damage processes of the UHPPFRC panel at elevated temperature.

$$c_{SO_4^{2-}} = c^i_{SO_4^{2-}} \tag{66}$$

where $c^i_{SO_4^{2-}}$ is a constant dependent on different cases in parametric study as shown in Table 2 ($i = 0, 1, 2$ representing the control case, Case 1 and Case 2, respectively). The sulphate concentrations are set as 2.5, 1, and 5 mol/m^3 in these three cases, respectively. At the other five surfaces, $c_{SO_4^{2-}}$ is set as zero.

2.4.2. Boundary conditions in heating stage

When exposed to elevated temperatures, face ABCD serves as the heating surface. The temperature T_h ($^\circ C$) is raised from the ambient temperature $20^\circ C$ to $600^\circ C$ at a heating rate of $2^\circ C/min$ as shown in Fig. 5 (b), where t is the heating time (min).

The pressure on the surface of the UHPPFRC panel is equal to the atmosphere pressure [21].

$$P_g = P_{g,\infty} \tag{67}$$

According to Ref. [18], the boundary condition for water vapor transfer at the panel surfaces is

$$\boldsymbol{n} \cdot \boldsymbol{J_v} = B_w \left(\rho_g^{sf} - \rho_{g,\infty} \right) \tag{68}$$

where $\boldsymbol{n}$ is the unit outward normal vector of the surface, $\boldsymbol{J_v}$ the water vapor flux vector, and B_w the surface emissivity for water vapor. ρ_g^{sf} and $\rho_{g,\infty}$ are the densities of water vapor at UHPPFRC panel surfaces and at adjacent environment, respectively. According to Ref. [21], a simplified boundary condition can be used by assuming $\boldsymbol{n} \cdot \frac{J_v}{B_w} = 0$, therefore, in the current study

$$\rho_g^{sf} = \rho_{g,\infty} \tag{69}$$

The boundary condition for heat transfer at UHPPFRC surfaces is given by Eq. (70) [20,68].

$$k_{eff}\frac{\partial T}{\partial n} + h_{qr}(T - T_\infty) + \lambda_e \, \boldsymbol{n} \cdot \boldsymbol{J_L} = 0 \tag{70}$$

where h_{qr} is the heat transfer coefficient, $h_{qr}(T - T_\infty)$ the heat energy dissipated by convection and radiation to the surrounding medium, $\lambda_e \, \boldsymbol{n} \cdot \boldsymbol{J_L}$ the heat energy used for evaporation of liquid water at boundary. Since the exposed surface of the UHPPFRC panel will become dry in a very short period of time when heating starts, the liquid fluid can be omitted, *i.e.* $(\boldsymbol{n} \cdot \boldsymbol{J_L}) = \boldsymbol{0}$, then the boundary condition can be simplified as

$$k_{eff}\frac{\partial T}{\partial n} + h_{qr}(T - T_\infty) = 0 \tag{71}$$

Furthermore, the displacement of the centre point of the UHPPFRC matrix, $\boldsymbol{u}(x = 150, y = 150, z = 60)$, consistently remains at zero.

2.4.3. Initial conditions

At $t = 0$, the concentrations of SO_4^{2-}, Ca^{2+}, hydrated calcium aluminates CA, and ettringite within UHPPFRC are

$$c_{SO_4^{2-}}(x, y, z, t = 0) = 0 \tag{72}$$

$$c_{Ca^{2+}}(x, y, z, t = 0) = c^{ini}_{Ca^{2+}} \tag{73}$$

$$c_{CA}(x, y, z, t = 0) = c^{ini}_{CA} \tag{74}$$

$$c_{ett}(x, y, z, t = 0) = 0 \tag{75}$$

Table 2
Different cases in parametric studies.

Cases	SO_4^{2-} concentration (mol/ m^3)	Heating rate ($^\circ C/min$)	Volume fraction of PP fibre (%)	Corrosion duration (years)
Control	2.5	2	0.33	5/10/15/20
1	1	2	0.33	
2	5	2	0.33	
3	2.5	1	0.33	
4	2.5	3	0.33	
5	2.5	2	0.22	
6	2.5	2	0.44	

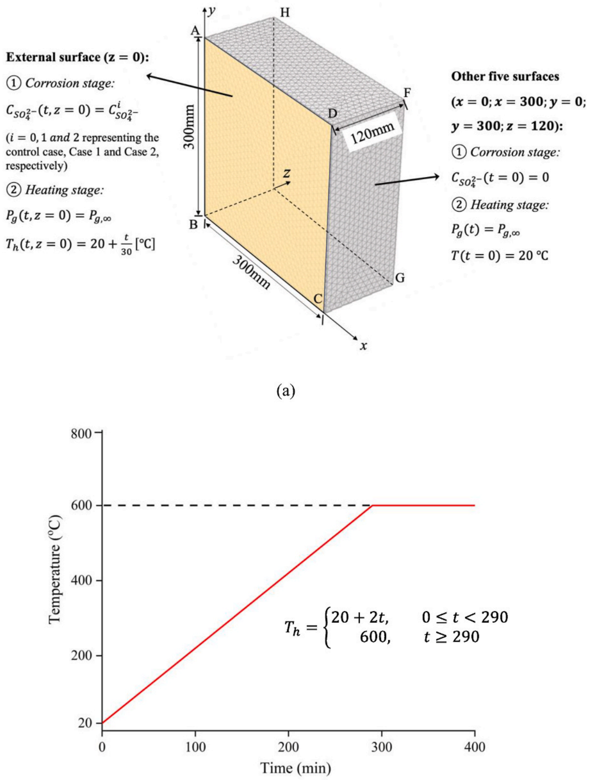

(a)

(b)

Fig. 5. Numerical model description, (a) boundary conditions and initial conditions, (b) the heating curve.

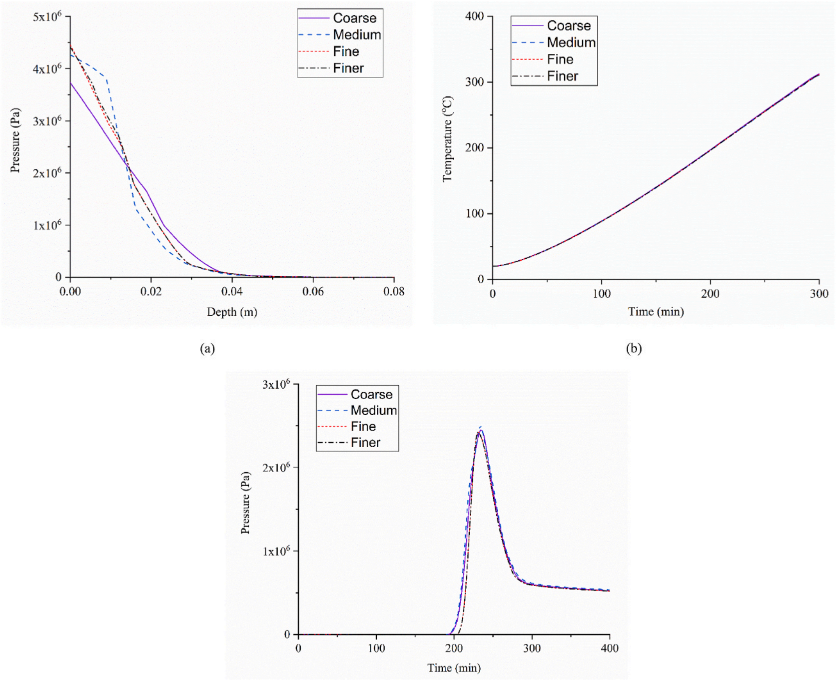

(a)

(b)

(c)

Fig. 6. Results of different parameters, (a) internal stress (b) temperature (c) pressure, predicted by different mesh densities in the convergency study.

3. Model validation

3.1. Mesh size analysis

Convergence study is carried out for the current model by using COMSOL Multiphysics. Referring to the recommended mesh size reported by Sun et al. [10] and Zhang et al. [9,25], four models with different mesh numbers, 1.2×10^4, 4.0×10^4, 8.8×10^4, and 1.5×10^5, are established for comparison, namely coarse, medium, fine and finer, respectively. The curves representing internal stress at corrosion stage, temperature at heating stage, and pore pressure at heating stages are shown in Fig. 6 (a) – 6 (c). The analysis results indicate that the predictions obtained by fine and finer models depict a similar trend and peak value. Thus, the fine model with a mesh number of 8.8×10^4 is chosen for both efficiency and accuracy. The corresponding maximum and minimum mesh size are 0.0127m and 0.0038m, respectively.

3.2. Model validation

Due to the lack of comprehensive research on the fire performance of aging UHPPFRC panels, validation of the present model is divided into two parts. The accuracy of the model in predicting the changes in internal expansive stress and porosity at corrosion stage is validated to ensure precise updates of UHPPFRC properties employed in the following heating stage. Meanwhile, the accuracy of temperature and stress distribution within UHPPFRC at heating stage is validated by comparing the current prediction with experimental measurements in the previous paper, thereby confirming that with the properties given, the present model can provide accurate predictions to investigate the fire resistance of UHPPFRC.

3.2.1. Corrosion stage

An UHPPFRC prism of 25 × 25 × 285 mm employed in Sun et al. [25] is established as the geometry in the present model, and the corresponding parameters and boundary conditions are set based on the experimental condition of immersing the specimen in 5 g/L sodium sulphate solution. The time dependent longitudinal expansion and porosity obtained in the simulation is then compared with the results given in Sun et al. [25].

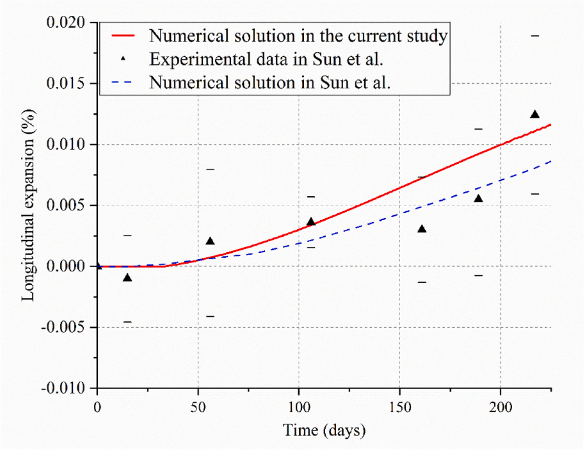

(a)

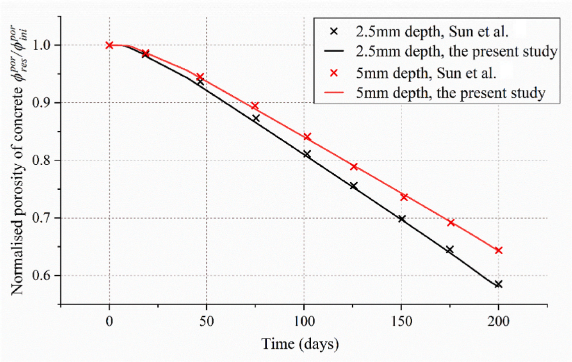

(b)

Fig. 7. Comparisons of longitudinal expansion and normalized porosity within UHPPFRC obtained by Sun et al. [25] and present model (a) internal stress, and (b) normalized porosity at different depths of UHPPFRC.

Fig. 7 (a) illustrates the comparison between the time-dependent longitudinal expansions of concrete bar predicted by the present model and from Sun et al.'s study [25]. Compared to the prediction in Sun et al. [25], the one given by the present model shows faster upward trend and fits better with the experimental measurements. Given that strain correlates to stress within linear elastic stage, it is thereby confirmed that the present model can accurately predict the internal stress within concrete throughout the corrosion stage. As shown in Fig. 7 (b), the change of normalized time-dependent porosity over time given by the current model also has a good agreement with those given in Sun et al. [25].

3.2.2. Heating stage

To verify the accuracy of the model in predicting temperature and stress at heating stage, the dimensions of the UHPPFRC panel in the present model is set as 300 × 300 × 120 mm based on the corresponding experimental setup in Li et al. [23], with the front 300× 300 mm face set as the heating surface.

Fig. 8 (a) and 8 (b) show the temperature and pore pressure predicted by the current model, and they are compared to the experimental measurements reported by Li et al. [23]. As can be seen, both curves from theoretical predictions and experimental measurements exhibit similar trends. In particular, the predicted peak pore pressures are only 5 % and 3 % higher than the test data at gauges P5 and P30, respectively. The slightly delayed occurrence of the predicted peak pore pressure at gauge P5 is caused by the lower temperature predicted at the same depth, while a little earlier occurrence of peak pore pressure at P30 is a result of the corresponding higher temperature prediction. Thus, the proposed model shows its ability to conservatively and accurately capture temperature and pore pressure distribution within the UHPPFRC panel at heating stage. Based on the comparison, the present model is considered to be highly suitable for the purpose of the current study to accurately predict the probability of failure and the crack propagation of aging UHPPFRC at elevated temperatures.

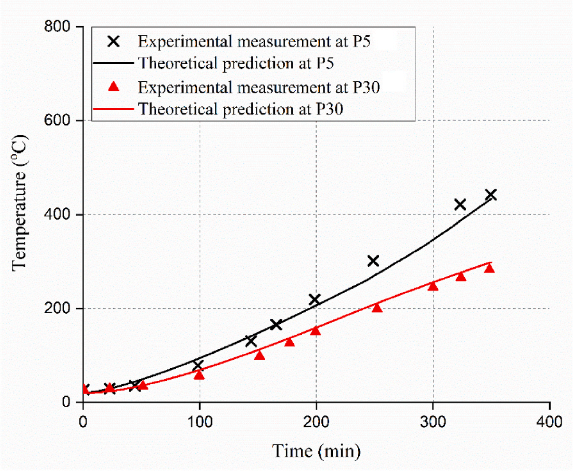

(a)

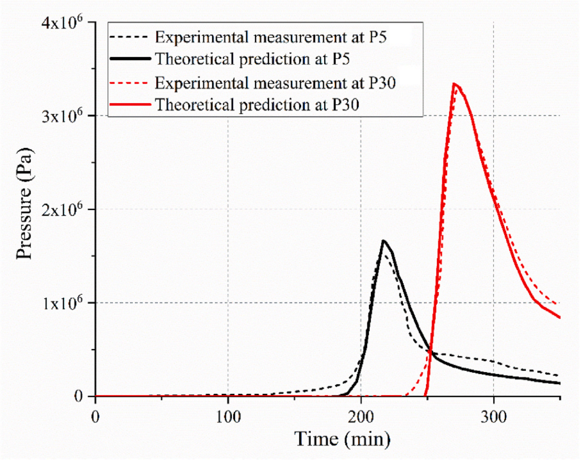

(b)

Fig. 8. Comparison between the tested temperature and pore pressure within the UHPPFRC panel in Li et al. [23] and the theoretical predictions (a) depth-dependent temperature, (b) depth-dependent pore pressure.

4. Parametric study

In this section, the influence of acid-rain-induced aging on the fire resistance of the UHPPFRC panel is firstly investigated. The probability of failure of the aging UHPPFRC panel predicted by the current model is compared to that of brand-new UHPPFRC panels and subsequently serves as the control case, in which the panel has the same dimension as the one demonstrated in Section 2.4. After that, a parametric study is carried out to explore the effects of different factors on the probability of failure and crack propagation in UHPPFRC panels with different degrees of aging. Five cases with various SO_4^{2-} concentration, heating rate and corrosion duration, namely Case 1 to 4 and the control case, are studied. The details of the five cases are listed in Table 2. Both internal stresses caused by corrosion and fire are considered, along with the application of reliability principles to account for the fluctuant performance of UHPPFRC panels. As the cracking phenomenon occurs at high temperature, the UHPPFRC panel transitions from linear elastic deformation stage to plastic deformation stage. This results in a permanent reduction in its tensile strength, corrosion rate increase, ultimately causing structural failure or an increased probability of failure. Therefore, in this section, the occurrence of crack at a specific depth in UHPPFRC is considered as an indicator of structure failure.

4.1. *Acid-rain-induced aging effect on the fire resistance of UHPPFRC*

According to previous studies [56,57], SO_4^{2-} concentration in acid rain can vary between 0.05 and 60 mol/m^3, depending on the region and specific country in the world. In previous research [44,69,70], 10 mol/m^3 is widely applied in acid rain corrosion experiments considering dry-wet cycle where various dry-wet modes and durations are chosen, while 1 to 60 mol/m^3 is employed in those considering continuous sulphate exposure. Therefore, as the first step towards to understanding the complex deterioration process, constant and continuous sulphate concentration, 1, 2.5 and 5 mol/m^3, are employed in this section. Among them, 2.5 mol/ m^3 is employed in the control case, in which a 120-month sulphate attack is introduced as the precondition for the following heating process with a heating rate of 2 $^\circ C$/min.

The investigation on the probability of failure of UHPPFRC at elevated temperatures is carried out with the consideration of the increasing internal expansive stress and the porosity change caused by corrosion over time. Fig. 9 (a) and 9 (b) show the comparison of probabilities of failure of UHPPFRC with and without corrosion at heating time $t_h = 30$ min and 40 min, respectively. As can be seen in Fig. 9 (a), P_f of UHPPFRC with corrosion demonstrates a rapid increasing trend, changing from 7 % (after 5-year corrosion) to 95 % (after 20-year corrosion), while P_f of UHPPFRC without corrosion remains consistently low, around 2.9 %, and does not vary with time. To be specific, the discrepancies in P_f between the results from the two models are 2.8 %, 17.9 %, 49.3 % and 90.9 % after 5, 10, 15 and 20 years, respectively. This maximum 25-fold discrepancy indicates that the aging effect can significantly reduce the fire resistance of UHPPFRC and increase its probability of failure at elevated temperatures. The stepwise increase of P_f also demonstrates

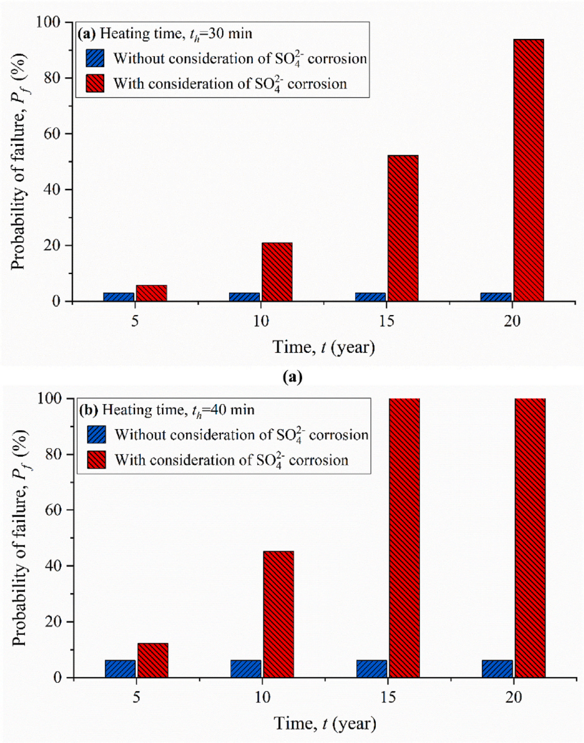

(a)

(b)

Fig. 9. Comparison of probability of failure between UHPPFRCs with and without corrosion, (a) at 30-min heating time (b) at 40-min heating time.

that the aging effect of UHPPFRC becomes more pronounced over time. Fig. 9 (b) depicts a similar trend, where P_f of UHPPFRC with 15-year corrosion reaches 100 % after 40-min heating, indicating its failure, while P_f of the brand new UHPPFRC is only 8 % at the same heating time.

In conclusion, aging effect significantly impairs the fire resistance of UHPPFRC. The ettringite accumulated during corrosion stage, as well as the decreasing porosity, might be responsible for this degradation. The accumulation of ettringite in pores generates internal expansive stress that weakens the tensile strength of UHPPFRC. Meanwhile, it can reduce porosity, which, in turn, increases pore pressure at elevated temperatures, causing an increased probability of failure.

4.2. Effect of external sulphate concentration

In practical, different regions may have different levels of SO_4^{2-} contamination and different precipitation, which means the sulphate concentration may change region by region. Therefore, the effect of external sulphate concentration on the aging effect of UHPPFRC should be further investigated.

In addition to the control case, two additional cases, Case 1 and Case 2, with reasonable sulphate concentrations of 1 mol/ m^3 and 5 mol/m^3 [56,57] respectively, are analysed in this section to investigate the effect of sulphate concentration on the fire performance and the probability of failure of UHPPFRC. All the other parameters remain the same.

Fig. 10 depicts the internal expansive stress $\boldsymbol{F_{ett}}$ within UHPPFRC at the end of the corrosion stage in the three cases. Evident differences among the calculated internal expansive stresses can be observed at the superficial area and gradually diminish with the increase in depth. At the surface, the internal stress in Case 1 is 74.0 % lower than that in the control case, while in Case 2, it is 71.2 % higher, indicating its rapidly increase with the growth of sulphate concentration. It should be noticed that the UHPPFRC panel in Case 2 almost reaches its tensile limit, resulting from the internal expansive stress generated by ettringite. The sulphate corrosion itself can lead to cracking of the UHPPFRC panel in Case 2 after around 13 years even without the following fire attack. This prediction is consistent with the previous study [25].

Fig. 11(a) and (b) show the probabilities of failure of the UHPPFRC panels with different sulphate concentrations at heating time $t_h = 30$ min and 40 min, respectively. P_fs of all three cases show increasing trends due to the increase of internal expensive stress caused by corrosion over time. As shown in Fig. 11, the concentration differences have a relatively minor impact on the fire resistance of UHPPFRC with 5-year corrosion, where the probabilities of failure P_fs of the control case, Case 1 and Case 2 are 3.3 %, 5.7 % and 18.2 %, respectively. For UHPPFRC panels exposed to sulphate corrosion environment for a longer duration, the sulphate concentration has a more significant effect on their fire resistance. To be specific, for those with 10-year sulphate corrosion, the UHPPFRC in Case 1, with a P_f of 4.9 %, demonstrates excellent fire performance after 30-min heating. In contrast, the UHPPFRC in Case 2, with a P_f of 84.9 %, indicates a high risk of cracking and structural failure at the same temperature. When the corrosion duration comes to 20 years, both P_fs of UHPPFRCs in the control case and Case 2 exceed 90 %, whereas that in Case 1 remains at a relatively low level (13.9 %). Similar trends could be observed at heating time of $t_h = 40$ min, as shown in Fig. 11 (b), where P_fs of the three UHPPFRCs increase due to the higher temerature.

Besides, for UHPPFRCs with 5-year corrosion, P_f in Case 1 increases by 3.7 % (rising from 3.3 % to 7.0 %) as the heating time t_h changes from 30min to 40min, while P_fs in the control case and Case 2 increase by 6.5 % (rising from 5.7 % to 12.2 %) and 18.1 % (rising from 18.2 % to 39.3 %), respectively. Similar but more significant discrepancies in P_f increments could be observed among UHPPFRCs with longer corrosion durations, indicating that higher sulphate concentration can accelerate the structural failure of UHPPFRC with the increase in temperature.

To further investigate the effect of sulphate concentration on UHPPFRC structures, comparisons of crack propagations in different cases are carried out. Fig. 12 shows the variation of tensile strains at a depth of 20 mm in UHPPFRCs for three cases, in which a normalized strain reaching 1 represents the occurrence of cracks. In the control case, Case 1 and Case 2, the cracks in UHPPFRC reach a

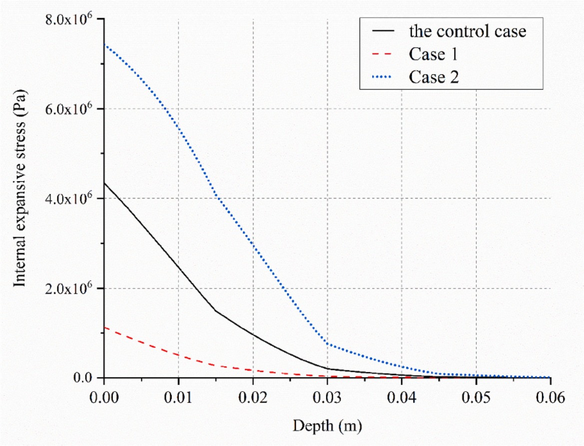

Fig. 10. Internal expansive stress at the end of the corrosion stage as a function of the depth with different sulphate concentrations.

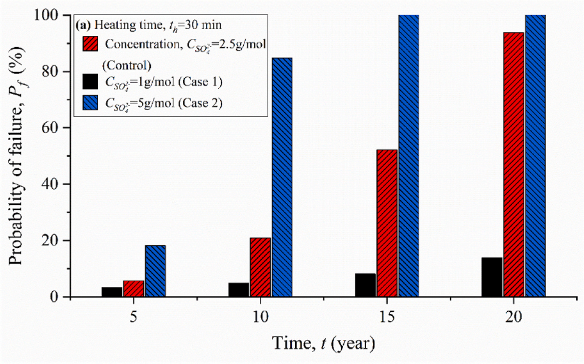

(a)

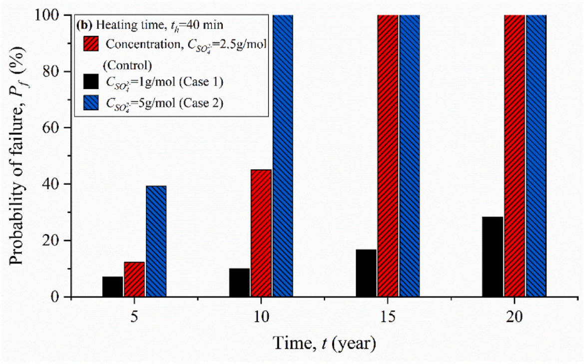

(b)

Fig. 11. Comparisons of failure probability of UHPPFRCs with different sulphate concentration at elevated temperatures, (a) after 30-min heating time; (b) after 40-min heating time.

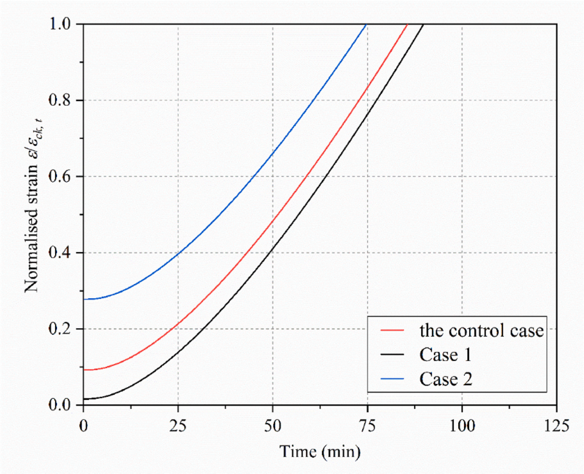

Fig. 12. The variation of tensile strain at 20 mm depths of UHPPFRC with 10-year corrosion.

depth of 20 mm at 85 min, 90 min and 75 min, respectively. Compared to the crack occurrence in the control case, the cracking time in Case 1 is postponed by 5.9 %, while in Case 2, it is advanced by 11.8 %.

On one hand, it can be observed that higher sulphate concentration leads to a greater initial tensile strain accumulated during the corrosion stage. Specifically, the initial tensile strains of the control case, Case 1 and Case 2 at 0 min indicate that the corresponding accumulated strains in the preceding corrosion stage are 0.09, 0.02 and 0.28, respectively. On the other hand, higher sulphate concentration can decrease the porosity of UHPPFRC by generating a larger amount of ettringite within pores, thereby further increasing the pore pressure accumulated within the pores at elevated temperatures. To investigate the extent of the effect of sulphate concentration on pore pressure, comparisons of pore pressure at a depth of 20 mm are carried out and shown in Fig. 13. As can be seen, pore pressures in different cases demonstrate subtle differences. Compared to the pressure peak in the control case, the ones in Case 1 and Case 2 only depict a 2 % decrease and a 2.8 % increase, respectively. This is because the melt of PP fibres during the heating, which is considered in the current model, can significantly increase the porosity of UHPPFRC [71], thus reducing the effect of ettringite formed by corrosion in decreasing the porosity. Moreover, the curves of pore pressure exhibit almost no upward trend before 230 min, indicating that pore pressure constitutes only a very small fraction of the overall internal stress when cracks occur at this depth in UHPPFRC, thereby lacking a decisive influence on crack propagation at elevated temperatures.

To sum up, the significant discrepancy in initial strains at heating time $t_h = 0$, which is determined by the sulphate concentration during the preceding corrosion stage, is the main factor affecting crack propagation in UHPPFRCs with varying degrees of aging at elevated temperature.

4.3. Effect of heating rate

The probability of failure of aging UHPPFRC may be influenced by heating rate. In fire behaviour experiments of concrete samples, constant and relatively low heating rates have been widely adopted to avoid premature cracking and spalling [72–74]. According to previous studies [12,75–77], the most commonly used temperature increase rates ranged from $1\ ^\circ C/min$ to $5^\circ C/min$. In this study, the heating rate of $2^\circ C/min$ is employed in the control case, and the heating rates of $1^\circ C/min$ and $3^\circ C/min$ are applied to Case 3 and Case 4, respectively.

The effect of heating rate on the probability of failure of aging UHPPFRC subjected to different heating time are shown in Fig. 14 (a) and 14 (b). As can be seen, a higher heating rate can accelerate the deterioration of the residual tensile strength of UHPPFRC by increasing the accumulation of thermal stress within aging UHPPFRC, thereby causing a higher probability of failure. Considering a 5-year corrosion period, when compared to the control case with a heating time of 30 min ($P_f = 5.7$ %), Case 3 exhibits a 2.7 % decrease, while Case 4 shows a 6.2 % increase. These two discrepancies increase with the extension of the corrosion duration. For instance, after a 10-year corrosion period, the corresponding discrepancies became -10.7 % (negative sign representing a decrease) and 25.2 %, respectively. When the corrosion duration reaches 15 years, UHPPFRC in Case 4 experiences inevitable failure after 30-min heating, while in Case 3, there is only a 25.2 % probability of failure at the same time. Moreover, when the heating rate is $1\ ^\circ C/\ min,$ the difference in probability of failure between UHPPFRC with 5-year corrosion and that with 15-year corrosion is approximately 20 %. With an increase in the heating rate to $3\ ^\circ C/min$, the corresponding difference rises to around 88 %.

Fig. 15 shows the variation of tensile strains in UHPPFRC panels over time at a depth of 20 mm under different heating rates. Heating rate has a significant impact on the initiation of crack formation. Compared to the control case, crack initiation is delayed by 51 min in Case 3 and advanced by 19 min in Case 4. To reach the same tensile strain, Case 3 and Case 4 show a 58 % delay and a 22 % acceleration respectively, compared to the control case throughout the entire process.

4.4. Effect of fibre dosage

In practice, the probability of failure in aging UHPPFRC is determined by both its load and tensile strength. In addition to the effects of load-related parameters like sulphate concentration and heating rate, the effect of fibre dosage is also investigated in the current study as a strength-related parameter. Three cases, the control case, Case 5 and Case 6, are introduced in this section. According to previous studies, fibre dosages between 0.1 % and 0.5 % have been widely employed for enhancing the fire behaviour of concrete [12], where 0.11%–0.44 % are adopted in many experiments [73,74,78–81]. Therefore, the corresponding fibre dosages are 0.33 %, 0.22 % and 0.44 %, respectively.

Fig. 16 (a) and 16 (b) demonstrate the probability of failure in UHPPFRC panels in three cases. It can be seen that Case 5, which has the lowest fibre dosage, consistently exhibits the highest probability of failure, regardless of the corrosion duration and heating time.

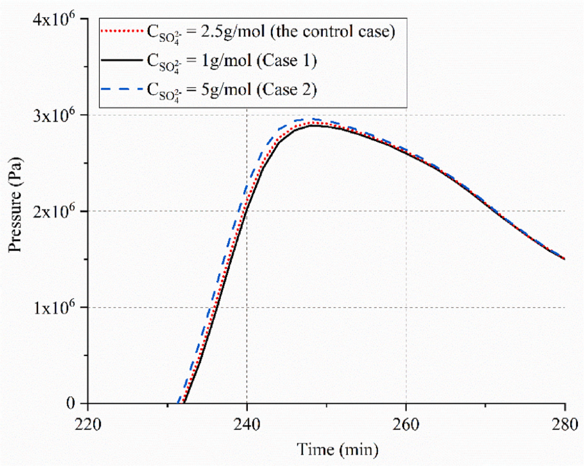

Fig. 13. Comparisons of pore pressures within UHPPFRCs subjected to different sulphate concentration at the depth of 20 mm.

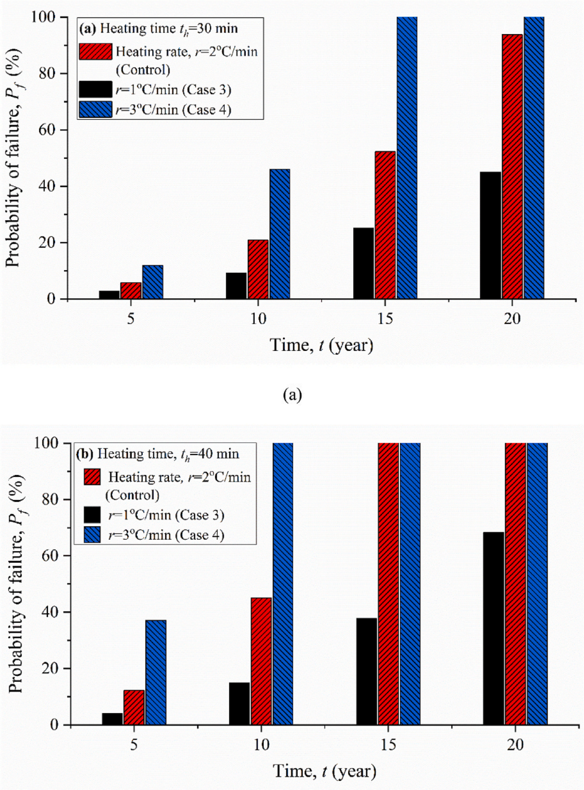

(a)

(b)

Fig. 14. Comparisons of failure probability of UHPPFRCs with different heating rate at elevated temperatures, (a) after 30-min heating time; (b) after 40-min heating time.

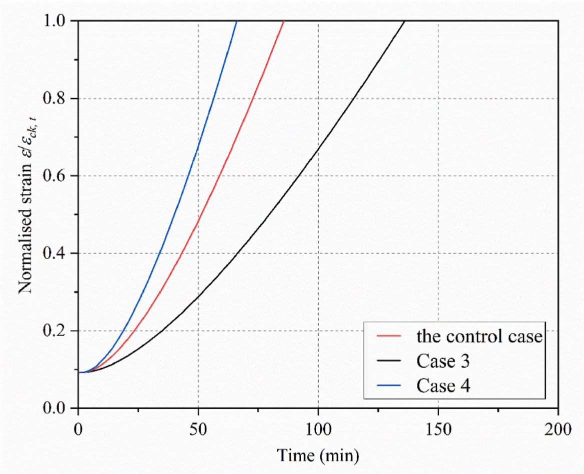

Fig. 15. Time dependent normalized maxiumum strain distribution at 20 mm depth of the UHPPFRC panel under different heating conditions.

Similar to other parameters, for UHPPFRC exposed to a longer duration of sulphate corrosion environment, fibre dosage has a more pronounced impact on its fire resistance. To be specific, when considering a 5-year corrosion period, all three cases have nearly identical probabilities of failure after 30-min heating. For UHPPFRC panels with longer corrosion durations, the discrepancies in the probability of failure become more evident, but the maximum probability of failure is still only 25 % (after 10-year corrosion). When the corrosion duration extends to 20 years, all three UHPPFRC panels fail after 30-min heating, regardless of the fibre dosage. As shown in Fig. 16 (b), at a heating time of 40 min, P_f of all three aging UHPPFRC panels with a 15-year corrosion period reach 100 %,

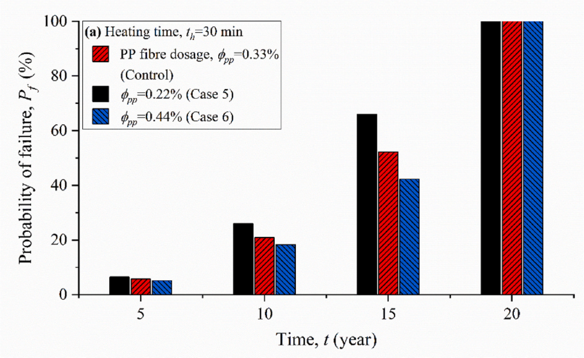

(a)

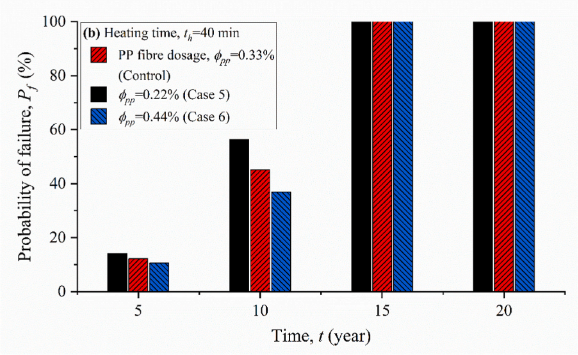

(b)

Fig. 16. Comparisons of failure probability of UHPPFRCs with different fibre dosages at elevated temperatures, (a) after 30-min heating time; (b) after 40-min heating time.

indicating their inevitable failure.

4.5. *Sensitivity study on different parameters*

Fig. 17 shows a spider plot to quantify the extent to which variations in different parameters affect the probability of failure in aging UHPPFRC with a 10-year corrosion period at elevated temperatures. All three parameters mentioned above (sulphate concentration, heating rate and fibre dosage) are compared to those in the control case. It can be seen that load-related parameters exhibit a positive correlation with the probability of failure, while the strength-related parameter, PP fibre dosage, shows a negative correlation. Under the same percentage of change, sulphate concentration $C_{SO_4^{2-}}$ demonstrates a greater impact on the probability of failure P_f than the

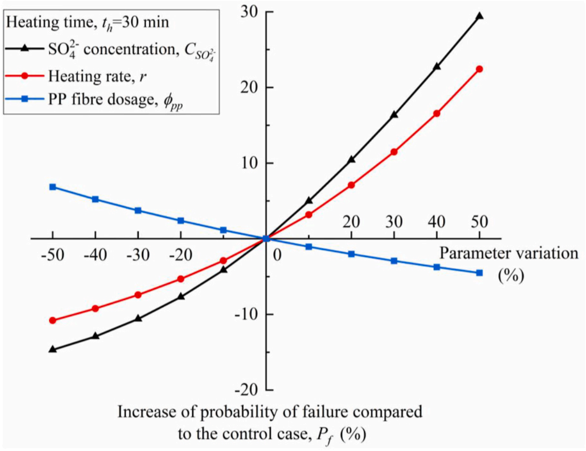

Fig. 17. Comparison of the sensitivities of probability of failure to different parameters.

heating rate *r*. When the two load-related parameters each increases by 50 %, the probability of failure in UHPPFRC subjected to higher sulphate concentration increases by an additional 10 % compared to the one subjected to a higher heating rate. On the other hand, the curve representing PP fibre dosage demonstrates the smallest slope in the figure, indicating that fibre dosage has a lesser impact on the probability of failure of UHPPFRC. This suggests that in practical applications, increasing the volume fraction of PP fibre can improve the aging resistance of UHPPFRC, but it is not a highly effective method. When fibre dosage increases by 50 %, the probability of failure of UHPPFRC decreases by 6 %.

5. Conclusions

In this study, a coupled chemo-thermal-mechanical model, incorporating the theory of porous media and Hill function, is proposed to investigate the fire resistance of aging UHPPFRC at linear elastic stage.

The deteriorating tensile strength and decreasing porosity of UHPPFRC panels under acid rain condition, which are mainly caused by the accumulation of reaction products within pores, are first derived with the consideration of the sulphate-related diffusion and reactions. By employing these updated properties, comparison between the fire performances of brand-new and aging UHPPFRC panels at elevated temperature is subsequently carried out, followed by the further investigation on the impact of sulphate concentration, heating rate and fibre dosage on the probability of failure and crack propagation of the aging UHPPFRC panels. The key findings of this research are drawn below.

1. The acid-rain-induced aging effect, mainly driven by the internal expansive stress caused by ettringite, can greatly impair the fire resistance of UHPPFRC, and this effect becomes more pronounced with an increase in the duration of corrosion. For UHPPFRC subjected to 20-year corrosion, its probability of failure after 30-min heating exceeds 90 %, whereas the brand new UHPPFRC only shows a probability of failure of 14 % at the same time.
2. The fire resistance of aging UHPPFRC deteriorates significantly with the rise in sulphate concentration. When the corrosion duration reaches 20 years, the probabilities of failure for both UHPPFRC panels with 2.5 mol/m^3 and 5 mol/m^3 sulphate concentrations exceed 90 %, whereas that with 1 mol/m^3 sulphate concentration remains at a relatively low level of 13.9 %. Therefore, different regions should establish corresponding UHPPFRC maintenance standards based on the local PH values. A lower PH value indicates the increase of hydrogen in acid rain, which usually accompanies an increase of sulphate ions.
3. The fire resistance discrepancy between UHPPFRC panels with different degrees of aging becomes more pronounced under a higher heating rate. At a heating rate of 1 $^\circ C/min$, the difference in the probability of failure between the UHPPFRC panel with 5-year corrosion and the one with 15-year corrosion is about 20 % after 30-min heating. However, with a heating rate of 3 $^\circ C/min$, the corresponding difference increases to around 88 %. This indicates the importance of UHPPFRC routine maintenance in acid-rain affected areas. Compared to brand new UHPPFRC panels, aged ones fail prematurely in real fire scenarios, where the heating rate is even higher.
4. The probability of failure of aging UHPPFRC is more sensitive to the changes in sulphate concentration than to changes in heating rate. Compared to these two factors, variations in PP fibre dosage have a less significant impact. In regions affected by acid rain, rather than simply employing a high-volume fraction of pp fibre, in combination with coating techniques or spraying alkaline solutions on the UHPPFRC panel to reduce sulphate concentration can better maintain its fire performance.

As an initial step towards understanding the complex acid-rain induced aging effect on the fire behaviour of the UHPPFRC panel, the current model still has some limitation requiring improvement and further discussion. For instance, given the complex deterioration process of UHPPFRC at elevated temperature, the change of internal expansive stress and porosity resulting from decompositions of the gypsum and ettringite during heating are not considered, leading to a more conservative prediction. Moreover, the heating rate in real fire scenarios, generally following the standard fire curve, is higher than the employed ones in the present study, which may cause a quick transition of the UHPPFRC panel from linear elastic to nonlinear stage, resulting in premature cracking and spalling. Furthermore, UHPPFRC panels subjected to corrosion and fire on opposite sides requires further investigation, as some fires affect the interior while acid rain primarily affects the external surface. These issues, together with the dimension- and shape-related factors, will be further studied and integrated into further models, allowing for a more comprehensive understanding.

CRediT authorship contribution statement

Boran Zhang: Writing – original draft, Validation, Software, Methodology, Investigation, Conceptualization. **Xiaoshan Lin:** Writing – review & editing, Supervision, Methodology. **Y.X. Zhang:** Writing – review & editing, Supervision, Methodology. **Lihai Zhang:** Writing – review & editing, Supervision, Methodology, Investigation, Conceptualization.

Declaration of competing interest

The authors declare that they have no known competing financial interests or personal relationships that could have appeared to influence the work reported in this paper.

Data availability

Data will be made available on request.

Acknowledgements

The authors acknowledge the funding support from The Australian Research Council (DP220103043) and The University of Melbourne.

References

[1] R. Yu, P. Spiesz, H.J.H. Brouwers, Mix design and properties assessment of ultra-high performance fibre reinforced concrete (UHPFRC), Cement Concr. Res. 56 (2014/02/01/2014) 29–39, https://doi.org/10.1016/j.cemconres.2013.11.002.

[2] D. Wang, C. Shi, Z. Wu, J. Xiao, Z. Huang, Z. Fang, A review on ultra high performance concrete: Part II. Hydration, microstructure and properties, Construct. Build. Mater. 96 (2015/10/15/2015) 368–377, https://doi.org/10.1016/j.conbuildmat.2015.08.095.

[3] J.-C. Mindeguia, P. Pimienta, A. Noumowé, M. Kanema, Temperature, pore pressure and mass variation of concrete subjected to high temperature — experimental and numerical discussion on spalling risk, Cement Concr. Res. 40 (3) (2010/03/01/2010) 477–487, https://doi.org/10.1016/j.cemconres.2009.10.011.

[4] C. Xu, D. Chen, S. Miramini, X. Liu, W. Xu, L. Zhang, Experimental fire performance assessment of a new type of prestressed composite circular precast concrete columns, Eng. Struct. 278 (2023/03/01/2023) 115509, https://doi.org/10.1016/j.engstruct.2022.115509.

[5] N. Han, J. Xiao, L. Zhang, Y. Peng, A microscale-based numerical model for investigating hygro-thermo-mechanical behaviour of 3D printed concrete at elevated temperatures, Construct. Build. Mater. 344 (2022) 128231, https://doi.org/10.1016/j.conbuildmat.2022.128231.

[6] Q. Ma, R. Guo, Z. Zhao, Z. Lin, K. He, Mechanical properties of concrete at high temperature—a review, Construct. Build. Mater. 93 (2015/09/15/2015) 371–383, https://doi.org/10.1016/j.conbuildmat.2015.05.131.

[7] M. Li, C. Qian, W. Sun, Mechanical properties of high-strength concrete after fire, Cement Concr. Res. 34 (6) (2004/06/01/2004) 1001–1005, https://doi.org/10.1016/j.cemconres.2003.11.007.

[8] Y. Li, E.-H. Yang, K.H. Tan, Effects of heating followed by water quenching on strength and microstructure of ultra-high performance concrete, Construct. Build. Mater. 207 (2019/05/20/2019) 403–411, https://doi.org/10.1016/j.conbuildmat.2019.02.123.

[9] B. Zhang, X. Lin, Y.X. Zhang, L. Zhang, Microscale failure analysis of the ultra-high-performance polypropylene fibre reinforced concrete panel subjected to high thermal loading induced by fire exposure, Eng. Struct. 292 (2023/10/01/2023) 116518, https://doi.org/10.1016/j.engstruct.2023.116518.

[10] Y. Ding, C. Zhang, M. Cao, Y. Zhang, C. Azevedo, Influence of different fibers on the change of pore pressure of self-consolidating concrete exposed to fire, Construct. Build. Mater. 113 (2016/06/15/2016) 456–469, https://doi.org/10.1016/j.conbuildmat.2016.03.070.

[11] G.-F. Peng, W.-W. Yang, J. Zhao, Y.-F. Liu, S.-H. Bian, L.-H. Zhao, Explosive spalling and residual mechanical properties of fiber-toughened high-performance concrete subjected to high temperatures, Cement Concr. Res. 36 (4) (2006/04/01/2006) 723–727, https://doi.org/10.1016/j.cemconres.2005.12.014.

[12] H. Wu, X. Lin, A. Zhou, A review of mechanical properties of fibre reinforced concrete at elevated temperatures, Cement Concr. Res. 135 (2020) 106117, https://doi.org/10.1016/j.cemconres.2020.106117.

[13] M.R. Bangi, T. Horiguchi, Pore pressure development in hybrid fibre-reinforced high strength concrete at elevated temperatures, Cement Concr. Res. 41 (11) (2011/11/01/2011) 1150–1156, https://doi.org/10.1016/j.cemconres.2011.07.001.

[14] P. Kalifa, G. Chéné, C. Gallé, High-temperature behaviour of HPC with polypropylene fibres: from spalling to microstructure, Cement Concr. Res. 31 (10) (2001/10/01/2001) 1487–1499, https://doi.org/10.1016/S0008-8846(01)00596-8.

[15] P. Kalifa, F.-D. Menneteau, D. Quenard, Spalling and pore pressure in HPC at high temperatures, Cement Concr. Res. 30 (12) (2000/12/01/2000) 1915–1927, https://doi.org/10.1016/S0008-8846(00)00384-7.

[16] Y. Li, D. Zhang, Effect of lateral restraint and inclusion of polypropylene and steel fibers on spalling behavior, pore pressure, and thermal stress in ultra-high-performance concrete (UHPC) at elevated temperature, Construct. Build. Mater. 271 (2021) 121879, https://doi.org/10.1016/j.conbuildmat.2020.121879.

[17] Z.P. Bažant, J.-C. Chern, W. Thonguthai, Finite element program for moisture and heat transfer in heated concrete, Nucl. Eng. Des. 68 (1) (1982/03/01/1982) 61–70, https://doi.org/10.1016/0029-5493(82)90040-1.

[18] Z.P. Bažant, W. Thonguthai, Pore pressure in heated concrete walls: theoretical prediction, Mag. Concr. Res. 31 (107) (1979) 67–76, https://doi.org/10.1680/macr.1979.31.107.67.

[19] D. Gawin, C.E. Majorana, B.A. Schrefler, Numerical analysis of hygro-thermal behaviour and damage of concrete at high temperature, Mech. Cohesive-Frict. Mater. 4 (1) (1999/01/01 1999) 37–74, https://doi.org/10.1002/(SICI)1099-1484(199901)4:1<37::AID-CFM58>3.0.CO;2-S.

[20] C.T. Davie, C.J. Pearce, N. Bićanić, Coupled heat and moisture transport in concrete at elevated temperatures—effects of capillary pressure and adsorbed water, Numer. Heat Tran., Part A: Applications 49 (8) (2006/09/01 2006) 733–763. https://www.tandfonline.com/doi/abs/10.1080/10407780500503854.

[21] R.T. Tenchev, L.Y. Li, J.A. Purkiss, Finite element analysis of coupled heat and moisture transfer in concrete subjected to fire, Numer. Heat Tran., Part A: Applications 39 (7) (2001) 685–710, https://doi.org/10.1080/10407780119853.

[22] P. Ren, X. Hou, V.K.R. Kodur, C. Ge, Y. Zhao, W. Zhou, Modeling the fire response of reactive powder concrete beams with due consideration to explosive spalling, Construct. Build. Mater. 301 (2021) 124094, https://doi.org/10.1016/j.conbuildmat.2021.124094.

[23] Y. Li, P. Pimienta, N. Pinoteau, K.H. Tan, Effect of aggregate size and inclusion of polypropylene and steel fibers on explosive spalling and pore pressure in ultra-high-performance concrete (UHPC) at elevated temperature, Cement Concr. Compos. 99 (2019/05/01/2019) 62–71, https://doi.org/10.1016/j.cemconcomp.2019.02.016.

[24] A. Neville, The confused world of sulfate attack on concrete, Cement Concr. Res. 34 (8) (2004/08/01/2004) 1275–1296, https://doi.org/10.1016/j.cemconres.2004.04.004.

[25] D. Sun, K. Wu, H. Shi, S. Miramini, L. Zhang, Deformation behaviour of concrete materials under the sulfate attack, Construct. Build. Mater. 210 (2019/06/20/2019) 232–241, https://doi.org/10.1016/j.conbuildmat.2019.03.050.

[26] S. Xu, et al., Experimental study of mechanical properties of G-UHPC against sodium sulfate attack at elevated temperature, Construct. Build. Mater. 396 (2023) 132387, https://doi.org/10.1016/j.conbuildmat.2023.132387.

[27] M. Kurtay, H. Gerengi, Y. Kocak, M.A. Chidiebere, M. Yildiz, The potency of zeolite and diatomite on the corrosive destruction of reinforcing steel in 1 M HNO3 environment, Construct. Build. Mater. 236 (2020) 117572, https://doi.org/10.1016/j.conbuildmat.2019.117572.

[28] V.E. García-Vera, M. Lanzón, Physical-chemical study, characterisation and use of image analysis to assess the durability of earthen plasters exposed to rain water and acid rain, Construct. Build. Mater. 187 (2018/10/30/2018) 708–717, https://doi.org/10.1016/j.conbuildmat.2018.07.235.

[29] Z. Liu, D. Deng, G.D. Schutter, Z. Yu, Micro-analysis of “salt weathering” on cement paste, Cement Concr. Compos. 33 (2) (2011/02/01/2011) 179–191, https://doi.org/10.1016/j.cemconcomp.2010.10.010.

[30] R. Tixier, B. Mobasher, Modeling of damage in cement-based materials subjected to external sulfate attack. I: formulation, J. Mater. Civ. Eng. 15 (4) (2003) 305–313, https://doi.org/10.1061/(ASCE)0899-1561(2003)15:4(305).

[31] R. Tixier, B. Mobasher, Modeling of damage in cement-based materials subjected to external sulfate attack. II: comparison with experiments, J. Mater. Civ. Eng. 15 (4) (2003) 314–322, https://doi.org/10.1061/(ASCE)0899-1561(2003)15:4(314).

[32] N. Cefis, C. Comi, Chemo-mechanical modelling of the external sulfate attack in concrete, Cement Concr. Res. 93 (2017/03/01/2017) 57–70, https://doi.org/10.1016/j.cemconres.2016.12.003.

[33] J.-k. Chen, C. Qian, H. Song, A new chemo-mechanical model of damage in concrete under sulfate attack, Construct. Build. Mater. 115 (2016/07/15/2016) 536–543, https://doi.org/10.1016/j.conbuildmat.2016.04.074.

[34] T. Ikumi, S.H.P. Cavalaro, I. Segura, A. Aguado, Alternative methodology to consider damage and expansions in external sulfate attack modeling, Cement Concr. Res. 63 (2014/09/01/2014) 105–116, https://doi.org/10.1016/j.cemconres.2014.05.011.

[35] A.E. Idiart, C.M. López, I. Carol, Chemo-mechanical analysis of concrete cracking and degradation due to external sulfate attack: a meso-scale model, Cement Concr. Compos. 33 (3) (2011/03/01/2011) 411–423, https://doi.org/10.1016/j.cemconcomp.2010.12.001.

[36] B. Bary, Simplified coupled chemo-mechanical modeling of cement pastes behavior subjected to combined leaching and external sulfate attack, Int. J. Numer. Anal. Methods GeoMech. 32 (14) (2008/10/10 2008) 1791–1816, https://doi.org/10.1002/nag.696.

[37] M. Basista, W. Weglewski, Micromechanical modeling of sulphate corrosion in concrete: influence of ettringite forming reaction, Theor. Appl. Mech. 35 (1–3) (2008) 29–52.

[38] S. Qin, D. Zou, T. Liu, A. Jivkov, A chemo-transport-damage model for concrete under external sulfate attack, Cement Concr. Res. 132 (2020/06/01/2020) 106048, https://doi.org/10.1016/j.cemconres.2020.106048.

[39] B. Bary, N. Leterrier, E. Deville, P. Le Bescop, Coupled chemo-transport-mechanical modelling and numerical simulation of external sulfate attack in mortar, Cement Concr. Compos. 49 (2014/05/01/2014) 70–83, https://doi.org/10.1016/j.cemconcomp.2013.12.010.

[40] P.N. Gospodinov, R.F. Kazandjiev, T.A. Partalin, M.K. Mironova, Diffusion of sulfate ions into cement stone regarding simultaneous chemical reactions and resulting effects, Cement Concr. Res. 29 (10) (1999/10/01/1999) 1591–1596, https://doi.org/10.1016/S0008-8846(99)00138-6.

[41] D. Sun, C. Huang, Z. Cao, K. Wu, L. Zhang, Reliability assessment of concrete under external sulfate attack, Case Stud. Constr. Mater. 15 (2021/12/01/2021) e00690, https://doi.org/10.1016/j.cscm.2021.e00690.

[42] L. Zhang, B.-S. Gardiner, D.-W. Smith, P. Pivonka, A. Grodzinsky, A fully coupled poroelastic reactive-transport model of cartilage, Molecular \& Cellular Biomechanics 5 (2) (2008) 133–154, https://doi.org/10.3970/mcb.2008.005.133.

[43] L. Zhang, B.S. Gardiner, D.W. Smith, P. Pivonka, A.J. Grodzinsky, On the role of diffusible binding partners in modulating the transport and concentration of proteins in tissues, Journal of Theoretical Biology 263 (1) (2010/03/07/2010) 20–29, https://doi.org/10.1016/j.jtbi.2009.11.023.

[44] K. Xu, L. Huang, L. Zhang, H. Xu, D. Zhu, P. Li, Experimental study on the seismic performance of prestressed concrete beams under low-cycle reciprocating load and simulated acid rain corrosion environment, Construction and Building Materials 408 (2023) 133629, https://doi.org/10.1016/j.conbuildmat.2023.133629.

[45] Y. Zhang, S. Zhuang, M. Qu, Q. Fang, Q. Zhao, G. Chen, Experimental study on compressive behavior of compressive stress-loaded concrete at different strain rates under simulated acid rain environment, Journal of Building Engineering 96 (2024/11/01/2024) 110584, https://doi.org/10.1016/j.jobe.2024.110584.

[46] M. Ozawa, Y. Sakoi, K. Fujimoto, K. Tetsura, S.S. Parajuli, Estimation of chloride diffusion coefficients of high-strength concrete with synthetic fibres after fire exposure, Construction and Building Materials 143 (2017/07/15/2017) 322–329, https://doi.org/10.1016/j.conbuildmat.2017.03.117.

[47] X. Liang, C. Wu, Y. Yang, C. Wu, Z. Li, Coupled effect of temperature and impact loading on tensile strength of ultra-high performance fibre reinforced concrete, Composite Structures 229 (2019/12/01/2019) 111432, https://doi.org/10.1016/j.compstruct.2019.111432.

[48] Maizuar, L. Zhang, R. Thompson, H. Fithra, Life-cycle performance of a bridge subjected to multiple heavy vehicle impacts, in: *Proceedings Of MICoMS 2017*, Vol. 1, (Emerald Reach Proceedings Series, Emerald Publishing Limited, 2018, pp. 13–18.

[49] S. Chen, C. Duffield, S. Miramini, B. Nasim Khan Raja, L. Zhang, Life-cycle modelling of concrete cracking and reinforcement corrosion in concrete bridges: a case study, Engineering Structures 237 (2021) 112143, https://doi.org/10.1016/j.engstruct.2021.112143.

[50] S. Shi, N. Lam, Y. Cui, G. Lu, E. Gad, L. Zhang, Life-cycle performance of aluminium cladding panels in resisting hailstorms, Structural Safety 108 (2024) 102439, https://doi.org/10.1016/j.strusafe.2024.102439.

[51] E.F. Irassar, Sulfate resistance of blended cement: prediction and relation with flexural strength, Cement and Concrete Research 20 (2) (1990/03/01/1990) 209–218, https://doi.org/10.1016/0008-8846(90)90073-7.

[52] M. Basista, W. Weglewski, Chemically assisted damage of concrete: a model of expansion under external sulfate attack, International Journal of Damage Mechanics 18 (2) (2009/03/01 2009) 155–175, https://doi.org/10.1177/1056789508097540.

[53] X.-B. Zuo, W. Sun, C. Yu, Numerical investigation on expansive volume strain in concrete subjected to sulfate attack, Construction and Building Materials 36 (2012/11/01/2012) 404–410, https://doi.org/10.1016/j.conbuildmat.2012.05.020.

[54] D. Sun, Z. Cao, C. Huang, K. Wu, G. De Schutter, L. Zhang, Degradation of concrete in marine environment under coupled chloride and sulfate attack: a numerical and experimental study, Case Studies in Construction Materials 17 (2022/12/01/2022) e01218, https://doi.org/10.1016/j.cscm.2022.e01218.

[55] V. Kodur, S. Banerji, R. Solhmirzaei, Effect of temperature on thermal properties of ultrahigh-performance concrete, Journal of Materials in Civil Engineering 32 (8) (2020/08/01 2020) 04020210, https://doi.org/10.1061/(ASCE)MT.1943-5533.0003286.

[56] Y. Yin, J. Zhang, G. Zhang, Effect of hygrothermal acid rain environment on the shear bonding performance of CFRP-concrete interface, Construction and Building Materials 364 (2023) 130002, https://doi.org/10.1016/j.conbuildmat.2022.130002.

[57] Y. Peng, X. Meng, F. Song, G. Xu, Experimental study on the corrosion characteristics of concrete exposed to acid water containing aggressive carbon dioxide and sodium sulfate, Construction and Building Materials 321 (2022) 126397, https://doi.org/10.1016/j.conbuildmat.2022.126397.

[58] J.R. Clifton, J.M. Pommersheim, Sulfate Attack of Cementitious Materials: Volumetric Relations and Expansions, National Institute of Standards and Technology, Gaithersburg, Maryland, 1994.

[59] M.B. Dwaikat, V.K.R. Kodur, Hydrothermal model for predicting fire-induced spalling in concrete structural systems, Fire Safety Journal 44 (3) (2009/04/01/2009) 425–434, https://doi.org/10.1016/j.firesaf.2008.09.001.

[60] L. Zhang, Solute transport in cyclic deformed heterogeneous articular cartilage, International Journal of Applied Mechanics 3 (3) (2011) 507–524, https://doi.org/10.1142/S175882511100110X.

[61] D. Sun, K. Wu, H. Shi, L. Zhang, L. Zhang, Effect of interfacial transition zone on the transport of sulfate ions in concrete, Construction and Building Materials 192 (2018/12/20/2018) 28–37, https://doi.org/10.1016/j.conbuildmat.2018.10.140.

[62] E.J. Garboczi, Permeability, diffusivity, and microstructural parameters: a critical review, Cement and Concrete Research 20 (4) (1990/07/01/1990) 591–601, https://doi.org/10.1016/0008-8846(90)90101-3.

[63] M.A.B. Promentilla, T. Sugiyama, T. Hitomi, N. Takeda, Quantification of tortuosity in hardened cement pastes using synchrotron-based X-ray computed microtomography, Cement and Concrete Research 39 (6) (2009/06/01/2009) 548–557, https://doi.org/10.1016/j.cemconres.2009.03.005.

[64] H.L. Zhang, C.T. Davie, A numerical investigation of the influence of pore pressures and thermally induced stresses for spalling of concrete exposed to elevated temperatures, Fire Safety Journal 59 (2013) 102–110, https://doi.org/10.1016/j.firesaf.2013.03.019.

[65] W. Kunther, B. Lothenbach, K.L. Scrivener, On the relevance of volume increase for the length changes of mortar bars in sulfate solutions, Cement and Concrete Research 46 (2013/04/01/2013) 23–29, https://doi.org/10.1016/j.cemconres.2013.01.002.

[66] L. Zhang, B.S. Gardiner, D.W. Smith, P. Pivonka, A.J. Grodzinsky, Integrated model of IGF-I mediated biosynthesis in a deformed articular cartilage, Journal of Engineering Mechanics 135 (5) (2009) 439–449, https://doi.org/10.1061/(ASCE)0733-9399(2009)135:5(439).

[67] C.G. Koh, K.K. Ang, L. Zhang, Effects of repeated loading on creep deflection of reinforced concrete beams, Engineering Structures 19 (1) (1997/01/01/1997) 2–18, https://doi.org/10.1016/S0141-0296(96)00028-4.

[68] B.N.K. Raja, S. Miramini, C. Duffield, M. Sofi, P. Mendis, L. Zhang, The influence of ambient environmental conditions in detecting bridge concrete deck delamination using infrared thermography (IRT), Structural Control and Health Monitoring 27 (4) (2020) e2506, https://doi.org/10.1002/stc.2506.

[69] L. Guo, W. Guo, D. Chen, K. Wang, L. Yu, Experimental study on reinforced concrete small-eccentricity compressive column after acid rain corrosion, Journal of Building Engineering 83 (2024/04/15/2024) 108331, https://doi.org/10.1016/j.jobe.2023.108331.

[70] L. Zhang, Y. Pan, K. Xu, L. Bi, M. Chen, B. Han, Corrosion behavior of concrete fabricated with lithium slag as corrosion inhibitor under simulated acid rain corrosion action, Journal of Cleaner Production 377 (2022) 134300, https://doi.org/10.1016/j.jclepro.2022.134300.

[71] J. Lin, Y. Zhang, Z. Guo, H. Du, Impact of synthetic fibers on spalling and intrinsic pore structure of ultra-high performance concrete (UHPC) under elevated temperatures, Construction and Building Materials 439 (2024) 137325, https://doi.org/10.1016/j.conbuildmat.2024.137325.

[72] C.-G. Han, Y.-S. Hwang, S.-H. Yang, N. Gowripalan, Performance of spalling resistance of high performance concrete with polypropylene fiber contents and lateral confinement, Cement and Concrete Research 35 (9) (2005/09/01/2005) 1747–1753, https://doi.org/10.1016/j.cemconres.2004.11.013.

[73] C.S. Poon, Z.H. Shui, L. Lam, Compressive behavior of fiber reinforced high-performance concrete subjected to elevated temperatures, Cement and Concrete Research 34 (12) (2004/12/01/2004) 2215–2222, https://doi.org/10.1016/j.cemconres.2004.02.011.

[74] X. Luo, W. Sun, S.Y.N. Chan, Effect of heating and cooling regimes on residual strength and microstructure of normal strength and high-performance concrete, Cement and Concrete Research 30 (3) (2000/03/01/2000) 379–383, https://doi.org/10.1016/S0008-8846(99)00264-1.

[75] W. Khaliq, V. Kodur, Thermal and mechanical properties of fiber reinforced high performance self-consolidating concrete at elevated temperatures, Cement and Concrete Research 41 (11) (2011/11/01/2011) 1112–1122, https://doi.org/10.1016/j.cemconres.2011.06.012.

[76] K.K. Sideris, P. Manita, E. Chaniotakis, Performance of thermally damaged fibre reinforced concretes, Construction and Building Materials 23 (3) (2009/03/01/2009) 1232–1239, https://doi.org/10.1016/j.conbuildmat.2008.08.009.

[77] Y. Ju, L. Wang, H. Liu, K. Tian, An experimental investigation of the thermal spalling of polypropylene-fibered reactive powder concrete exposed to elevated temperatures, Science Bulletin 60 (23) (2015/12/01/2015) 2022–2040, https://doi.org/10.1007/s11434-015-0939-0.

[78] P. Pliya, A.L. Beaucour, A. Noumowé, Contribution of cocktail of polypropylene and steel fibres in improving the behaviour of high strength concrete subjected to high temperature, Construction and Building Materials 25 (4) (2011/04/01/2011) 1926–1934, https://doi.org/10.1016/j.conbuildmat.2010.11.064.

[79] Y. Li, K.H. Tan, E.-H. Yang, Synergistic effects of hybrid polypropylene and steel fibers on explosive spalling prevention of ultra-high performance concrete at elevated temperature, Cement and Concrete Composites 96 (2019/02/01/2019) 174–181, https://doi.org/10.1016/j.cemconcomp.2018.11.009.

[80] Y.N. Chan, X. Luo, W. Sun, Compressive strength and pore structure of high-performance concrete after exposure to high temperature up to 800°C, Cement and Concrete Research 30 (2) (2000/02/01/2000) 247–251, https://doi.org/10.1016/S0008-8846(99)00240-9.

[81] J. Eidan, I. Rasoolan, A. Rezaeian, D. Poorveis, Residual mechanical properties of polypropylene fiber-reinforced concrete after heating, Construction and Building Materials 198 (2019/02/20/2019) 195–206, https://doi.org/10.1016/j.conbuildmat.2018.11.209.

[82] D. Xu, et al., Influence of silica fume and thermal curing on long-term hydration, microstructure and compressive strength of ultra-high performance concrete (UHPC), Construction and Building Materials 395 (2023) 132370, https://doi.org/10.1016/j.conbuildmat.2023.132370.

[83] C. Sun, J. Chen, J. Zhu, M. Zhang, J. Ye, A new diffusion model of sulfate ions in concrete, Construction and Building Materials 39 (2013/02/01/2013) 39–45, https://doi.org/10.1016/j.conbuildmat.2012.05.022.

[84] Y. Zhang, et al., An improved micromechanical model for the thermal conductivity of multi-scale fiber reinforced ultra-high performance concrete under high temperatures, Materials & Design 236 (2023/12/01/2023) 112503, https://doi.org/10.1016/j.matdes.2023.112503.

[85] L. Shen, et al., On the moisture migration of concrete subject to high temperature with different heating rates, Cement and Concrete Research 146 (2021/08/01/2021) 106492, https://doi.org/10.1016/j.cemconres.2021.106492.